

Directed percolation and puff jamming near the transition to pipe turbulence

Received: 14 October 2022

Accepted: 16 April 2024

Published online: 27 May 2024

 Check for updates


Grégoire Lemoult ^{1,2}, Vasudevan Mukund², Hong-Yan Shih ^{3,4,5},
Gaute Linga ^{6,7}, Joachim Mathiesen ⁶, Nigel Goldenfeld ^{3,8}  &
Björn Hof ² 

The onset of turbulence in pipe flow has defied detailed understanding ever since the first observations of the spatially heterogeneous nature of the transition. Recent theoretical studies and experiments in simpler, shear-driven flows suggest that the onset of turbulence is a directed-percolation non-equilibrium phase transition, but whether these findings are generic and also apply to open or pressure-driven flows is unknown. In pipe flow, the extremely long time scales near the transition make direct observations of critical behaviour virtually impossible. Here we find a technical solution to that limitation and show that the universality class of the transition is directed percolation, from which a jammed phase of puffs emerges above the critical point. Our method is to experimentally characterize all pairwise interactions between localized patches of turbulence puffs and use these interactions as input for renormalization group and computer simulations of minimal models that extrapolate to long length and time scales. The strong interactions in the jamming regime enable us to explicitly measure the turbulent fraction and confirm model predictions. Our work shows that directed-percolation scaling applies beyond simple closed shear flows and underscores how statistical mechanics can lead to profound, quantitative and predictive insights on turbulent flows and their phases.

The behaviour of basic fluid flows is governed by the Reynolds number, $Re \equiv UD/\nu$, where U is a characteristic velocity, which in pipe flow we will take to be the bulk velocity, D is a length scale that we will take to be the pipe diameter and ν is the kinematic viscosity. At low Re , below about 2,000 in pipes, fluid flow is smooth and predictable (that is, laminar), but it becomes irregular, stochastic and unpredictable (that is, turbulent) at higher Re . At the onset of turbulence in pipe flow, spatially localized patches of turbulence (puffs) emerge from the laminar background flow, as first reported by Reynolds¹ and subsequently studied in detail^{2–6}. Puffs

have finite lifetimes and decay following a memoryless process^{7–11}. Before decay, and depending on the Reynolds number, they can seed other puffs through a process called puff splitting. Based on these observations, the critical point (that is, the critical Reynolds number Re_c) for the onset of sustained turbulence can be approximated by the Reynolds number where puff decay and splitting are balanced, so that there is a non-zero turbulent fraction in the pipe¹². Theory suggests that this transition might generally be described as a non-equilibrium phase transition in the directed percolation (DP) universality class^{11,13–20}, and experiments

¹LOMC, CNRS UMR 6294, Université Le Havre Normandie, Le Havre, France. ²Institute of Science and Technology Austria, Klosterneuburg, Austria.

³Department of Physics, University of Illinois at Urbana-Champaign, Loomis Laboratory of Physics, Urbana, IL, USA. ⁴Institute of Physics, Academia Sinica, Taipei, Taiwan. ⁵Physics Division, National Center for Theoretical Sciences, Taipei, Taiwan. ⁶Niels Bohr Institute, University of Copenhagen, Copenhagen, Denmark. ⁷PoreLab, The Njord Centre, Departments of Physics and Geosciences, University of Oslo, Oslo, Norway. ⁸Department of Physics, University of California San Diego, La Jolla, CA, USA.  e-mail: nigelg@ucsd.edu; bhof@ist.ac.at

in closed quasi-one-dimensional²¹ and two-dimensional²² Taylor–Couette flows have measured critical exponents and universal scaling functions in satisfactory agreement with expectations.

The main practical difficulty in determining the nature of the laminar–turbulent transition in shear flows is the excessively long time scale of the underlying microscopic processes. Near the transition in pipe flow, puff decay and splitting have time scales that are of order 10^7 advective time units (D/U) (ref. 12). The time scales of flow patterns to reach a statistical steady state diverge as the critical point is approached, and even a finite distance away from the critical point will far exceed the respective life and splitting times. In this regard, transitional turbulence is plagued with the problems of huge time and length scales that arise in other areas of physics, including equilibrium phase transitions²³ and the glass transition²⁴. Given that turbulent puffs advect downstream at approximately the bulk flow speed, pipes considerably exceeding 10^7 diameters in length would be required to investigate the nature of the transition, making such an undertaking impossible in practice.

Although these requirements may appear to put a solution to the pipe flow problem beyond reach, we here present a way to circumvent these practical limitations. Specifically, we precisely measure the different phenomena occurring at the scale of individual puffs and then perform up-scaling by combining the experimental data with theory and numerical simulations to reveal the statistical nature of the transition and the phase diagram of interacting turbulent puffs. In Fig. 1, we summarize our bottom-up multiscale approach. At the lowest level of description, experiment and also direct numerical simulations (DNSs) reveal that puffs move and interact^{25,26} through four elemental processes that we measure in detail here: (1) ‘pushing’ of a downstream puff by its upstream neighbour; (2) ‘suppression’ of a downstream puff by its upstream neighbour, causing it to decay faster than it would in isolation; (3) ‘inhibition’ of the splitting of an upstream puff by the presence of a sufficiently close downstream neighbour; and (4) random motion of a puff superimposed on the mean flow velocity downstream. From these ingredients, we develop long-wavelength model equations of motion on scales larger than the puff dimensions for a system of effectively point-like interacting puffs that can be solved numerically. At the highest level of description, we formulate the statistical mechanics for the model of interacting puffs and solve for the phase diagram and universality class using renormalization group theory and coarse-grained numerical methods. Finally the model predictions are verified in experiments using a new technique to periodically re-create puff patterns, allowing observation times in excess of the limit set by the physical pipe length. The point-puff approximation is justified by our measurements and simulations of puff turbulent energy profiles, showing localization over a length scale that does not diverge going through the transition region and implying that the origin of critical scaling behaviour is the collective, system-wide interactions of the puffs on large length scales (see Supplementary Information Section I for more discussion).

To characterize quantitatively the puff–puff interactions, experiments were carried out, in which puffs were generated near the inlet of a pipe and monitored at several locations downstream using pressure sensors. A detailed description of the setup and procedure is available in Supplementary Information Section I. In subsequent discussion of the experiments, quantities are non-dimensionalised by using the pipe diameter D and mean velocity U as the length and velocity scales.

We first investigated the repulsion mechanism between puffs. Two different protocols were used to measure how the puff advection speed is influenced by an upstream puff. In the first series of experiments, two puffs were generated. A first pressure sensor detects them $75 D$ downstream, and then a second sensor detects them a further $350 D$ downstream. The time delay for each puff gives us its speed, and the time delay between them gives us the puff separation. These experiments confirmed that the upstream puff speed was unaffected by the presence of the downstream puff, and its velocity was consistent with the speed of an isolated puff measured previously²⁷.

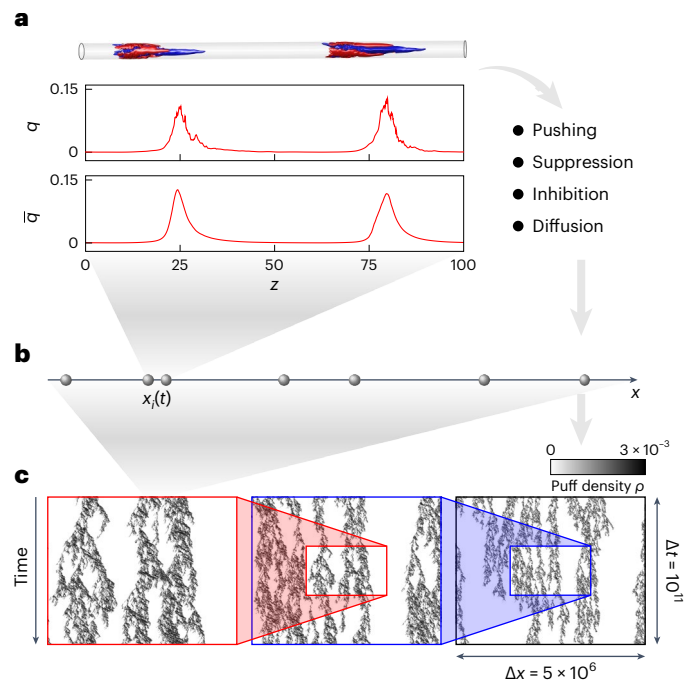


Fig. 1 | Illustration of the bottom-up multiscale approach to the laminar–turbulent transition in pipe flow used in this study. a, Instantaneous turbulent kinetic energy of the perturbation averaged over the cross-section of the pipe $q(z, t) = \int (\mathbf{u} - \mathbf{u}_{\text{lam}})^2 d^2 \mathbf{r}$ from a DNS showing two interacting turbulent puffs. \mathbf{u} is the velocity field as a function of space \mathbf{r} , z is the streamwise direction along the pipe axis, d is a notation from calculus and \mathbf{u}_{lam} is the laminar velocity field. Its time-averaged (in a comoving frame) value, \bar{q} , shows that although each puff is unique due to its history and dynamics, the time-averaged counterparts are statistically equivalent. The spatially localized turbulent kinetic energy justifies the point-like particle approach. **b**, A mesoscale model describes puffs as point particles interacting in a one-dimensional domain and is solved numerically. **c**, At the macroscopic scale, statistical mechanics analytically and numerically yields the phase diagram and detailed transitional behaviour of the flow. Here scale invariance at the critical point is illustrated in our continuous model using the puff density ρ in a large domain for $\text{Re} = 2,040.22$ ($\text{Re} - \text{Re}_c = 0.004$).

However, the speed of the downstream puff was different from that of an isolated puff, and could not be calculated from this experiment. Instead, a second protocol was used, which consisted of triggering a train of 100 equally spaced puffs and measuring the time delays between two pressure sensors separated by $350 D$. The advantage here is that the distance between two puffs does not vary during the experiment. In both protocols, if a splitting or decay event was detected, the measurement was discarded. We averaged these measurements over 1,000 realizations for the first protocol and 10 realizations for the second protocol, effectively averaging over the same number of puffs. The outcomes of these experiments are summarized in Fig. 2.

Figure 2a presents the evolution of the downstream puff velocity, $v_{\text{puff}}(l)$, as a function of the upstream puff distance l . For each Re , we observe a plateau for $l > 100$ corresponding to the advection speed of an isolated puff, v_{∞} . For $l < 100$, the downstream puff is accelerated corresponding to a repulsion. By transforming to the frame moving at v_{∞} , it is possible to collapse all curves into a unique one. We fitted these master curves by an exponential decay

$$v_{\text{puff}}(l) - v_{\infty} = A \exp(-l/l_c), \quad (1)$$

with amplitude $A = 0.22$ and decay length $l_c = 12$. The exponential nature of the interaction confirms that the puff–puff repulsion is only short-range.

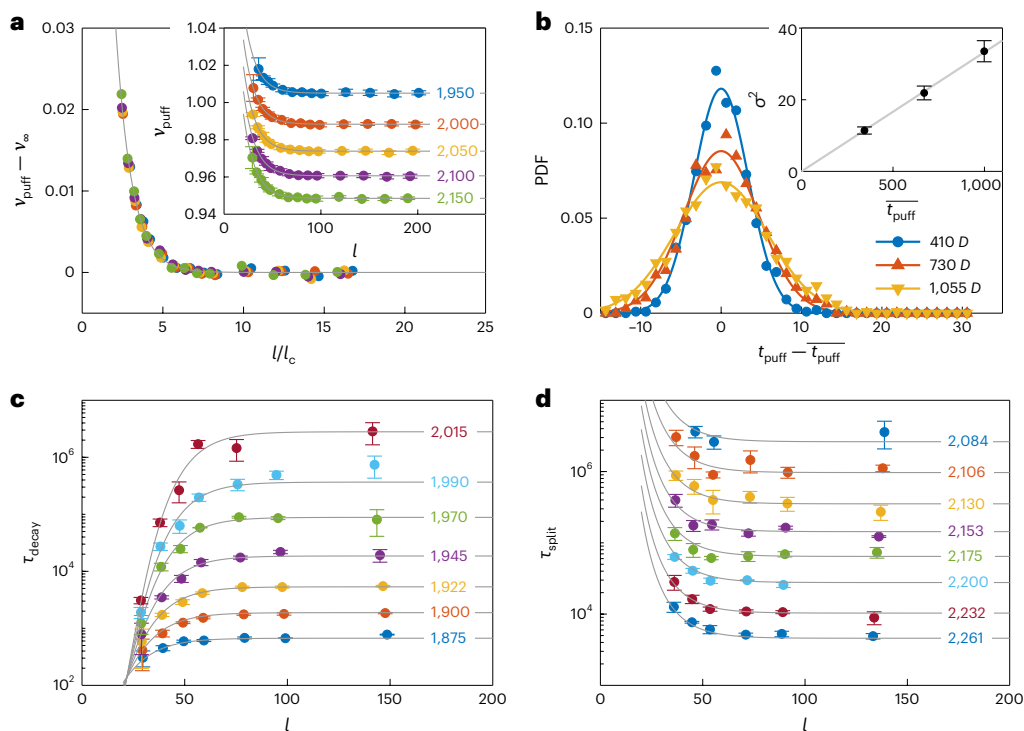


Fig. 2 | Puff dynamics as a function of puff-to-puff separation and Re. **a**, Speed of a puff as a function of the distance l to an upstream puff for different Re (indicated in the figure). Data are presented as mean values \pm s.d. over 10 realizations of a 100-puff train. Curves are collapsed by subtracting the advection speed of an isolated puff as measured by ref. 27. The grey solid line is the best fit for the collapsed data by an exponential decay ($v_{\text{puff}}(l) - v_{\infty} = A \exp(-l/l_c)$) with amplitude $A = 0.22$ and decay length $l_c = 12$. **b**, Time of arrival (t_{puff}) distributions (1,000 puffs) for different positions along the pipe axis for $\text{Re} = 2,040$. Solid lines are the best fit by a normal distribution. An isolated puff effective diffusion coefficient, D_{puff} , is estimated from the evolution of the variance of the probability density functions (PDFs) (inset), where error bars represent the 95%

confidence interval. **c**, Evolution of the characteristic decay time (τ_{decay}) for different Re (for values, see figure) as a function of the distance to an upstream puff. **d**, Evolution of the characteristic splitting time (τ_{split}) for different Re (for values, see figure) as a function of the distance l to a downstream puff. In **c** and **d**, the grey solid lines are the interpolation function used in the model (see Supplementary Information Section II for more details). Decay/splitting times are presented as their best estimate \pm their 95% confidence interval obtained by fitting the decay/splitting distribution with a Poisson distribution. The distribution sample size varies for each (Re , l) and is thus given in Supplementary Tables 1 and 2.

We then investigated how the presence of a second puff influences the characteristic times associated with decay and splitting. For this series of experiments, we used four pressure sensors located at $75 D$, $410 D$, $730 D$ and $1,055 D$ from the perturbation. A train of 1,000 equally spaced puffs was generated, and we monitored the number of decaying and splitting puffs at each sensor. We could confirm that both processes are memoryless by fitting the survival and splitting distributions with an exponential distribution; see Supplementary Information Section I for details of this procedure. The characteristic time of each distribution gives us the decay time (or splitting time) for this Re and puff-puff distance l .

Figure 2c shows the evolution of the characteristic decay times for different Re as a function of l . Once again these characteristic times reach a plateau for $l > 100$ corresponding to the isolated puff limit¹². For $l < 100$, the lifetime of a puff is considerably reduced (more than two orders of magnitude for $\text{Re} = 2,015$). Thus, the upstream puff is acting as a ‘puff killer’, as shown previously²⁵. The opposite situation arises in the splitting time of a puff (Fig. 2d). Although we still reach the isolated puff limit when $l > 100$, for $l < 100$, the presence of a downstream puff increases the characteristic splitting time, thus effectively inhibiting splitting.

Although puff propagation speed has been previously investigated²⁷, little is known of its stochastic nature. We recorded the arrival-time distribution of 1,000 isolated puffs using pressure sensors located at $75 D$, $410 D$, $730 D$ and $1,055 D$ downstream of the perturbation, using the first sensor as the time origin. Figure 2b shows those

distributions close to the transition at $\text{Re} = 2,040$. Their variance, σ^2 , shows a linear increase with time showing that puff propagation has a diffusive component in addition to the mean advection. We also determined how the puff diffusion coefficient, D_{puff} , varies with Re (Supplementary Fig. 12). However, it shows only a very weak dependence for $\text{Re} > 2,000$. Accordingly, for the analysis of the critical behaviour, we henceforth ignore its dependence on Re and use a fixed value of 0.015.

Having determined the pairwise interactions between puffs, we proceed to build a statistical mechanics model of their collective behaviour, treating each puff as a point particle. A similar philosophy, using numerical data, has been used to study boundary layer dynamics through a cellular automaton²⁸. A general configuration will be a gas of puffs with spatial density $\rho(x, t)$ at a position along the pipe with axis x and time t (see Supplementary Information Section III for a precise definition and analysis). The spatially averaged density (that is, a proxy for the turbulent fraction) along a pipe of length L is given by $\rho(t) \equiv \int_0^L \rho(x) dx/L$, and the long-time steady-state equilibrium value ρ_{∞} is expected to approach zero for $\text{Re} \rightarrow \text{Re}_c^+$ in the case of a continuous transition. Above and near the transition, $\rho_{\infty} \approx (\text{Re} - \text{Re}_c)^{\beta}$ asymptotically as $\text{Re} \rightarrow \text{Re}_c$. The critical exponent β has the value 0.276 for $1 + 1$ DP. We calculate the behaviour of $\rho(x, t)$ by first ignoring puff suppression or pushing. Particles can hop to positive x with rate p , decay with rate ω_d and split with rate ω_s . In this case, the time-dependent density $\rho(x, t)$ satisfies a stochastic hydrodynamics equation obtained by systematic expansion methods from the microscopic description of the above processes (Supplementary Information Section IV)

$$\begin{aligned} \partial_t \rho = & -\omega_d \rho + \frac{1}{2}(\rho + \omega_s) \partial_x^2 \rho - (\rho + \omega_s) \partial_x \rho + \omega_s \rho(1 - \rho) \\ & + (2\rho + \omega_s) \rho \partial_x \rho - \frac{\omega_s}{2} \rho \partial_x^2 \rho + \sqrt{\rho(1 - \rho)} \eta \end{aligned} \quad (2)$$

where $\eta(x, t)$ is a white noise delta-correlated in space and time, ρ is the rate at which particles hop to the right, ω_d is the puff decay rate and ω_s is the rate of puff splitting. Note that the calculation shows that the dynamics is controlled by multiplicative noise, which has the effect that the empty state is absorbing. This form of the noise arises because of the rule that there can be only one particle per site, corresponding to the fact that two puffs cannot occupy the same position in space. The description here is complementary to a recent stochastic account of puff interactions and their internal dynamics, extending to higher Re where expanding regions of turbulence occur²⁹.

Equation (2) is similar to the Langevin equation for DP³⁰, but with the addition of three terms: the term proportional to $\partial_x \rho$ and the last two terms of second order in ρ . The linear term arises because the puff dynamics is diffusive (the second-order term, linear in ρ) but in a frame moving with the net velocity of the puffs. This anisotropic diffusion can be removed by a Galilean transformation into the comoving frame. The second term is proportional to $\rho \partial_x \rho$ and has the functional form of the advective nonlinearity in Burgers equation. Such terms naturally arise in traffic-flow models³¹ and, loosely speaking, lead to shocks that model the bunching up of particles as occurs in traffic jams, transcription by ribosomes moving on mRNA^{32–34}, and so on. The shocks are regularized by the higher-order derivative terms, including the third extra term and the linear diffusive term. The connection to Burgers equation for the description of density dynamics in one-dimensional traffic-flow problems is standard and goes back to the earliest papers³⁵. Puff suppression and pushing add further higher-order and nonlinear terms to the equation of the form $\rho^\alpha (\partial_x^\beta \rho)^\gamma$ where α, β and γ are positive integers derived in Supplementary Information Section IV. This type of model is known to comprise rich dynamics, including jammed, crystalline phases where due to pushing, constituents are in close proximity and densely spaced. In the case of pipe flow, we would on this basis expect to observe crystalline regions that are separated by low-density regions where puffs freely advect and diffuse: in other words, a coexistence of fluid–crystalline regions. Close to the critical point, where the turbulent fraction is vanishingly small, the jammed crystalline regions are melted by fluctuations and do not influence the critical scaling behaviour. We discuss below the actual observations of this behaviour in both experiments and simulations. By writing the stochastic equation for $\rho(x, t)$ as a field theory and evaluating the scaling dimensions of all the terms at the fixed point describing the DP transition, we find that all the non-DP terms are irrelevant in the renormalization group sense (Supplementary Information Section IV). Therefore, the complicated dynamics of the puffs that we have characterized should behave asymptotically close to the onset of turbulence with the scaling behaviour of DP.

To test these theoretical predictions, we have performed a continuum stochastic dynamics simulation with a great level of realism regarding the interactions between puffs, as determined experimentally. In this continuum model, each puff is considered a point particle interacting with its closest neighbours, using the measured effective potential between puffs. We can then solve the equation of motion for each puff in the frame comoving at v_∞

$$\frac{dx_i}{dt} = v_{\text{puff}}(x_i - x_{i-1}) + \sqrt{2D_{\text{puff}}} \xi_i(t) \quad (3)$$

where x_i is the streamwise coordinate of the i th puff, $v_{\text{puff}}(x_i - x_{i-1})$ is the pushing speed of puff i as a result of puff $i - 1$ as measured in equation (1), and $\xi_i(t)$ is a Gaussian white noise with mean zero and standard deviation 1, thus modelling the random walk of an isolated puff due to

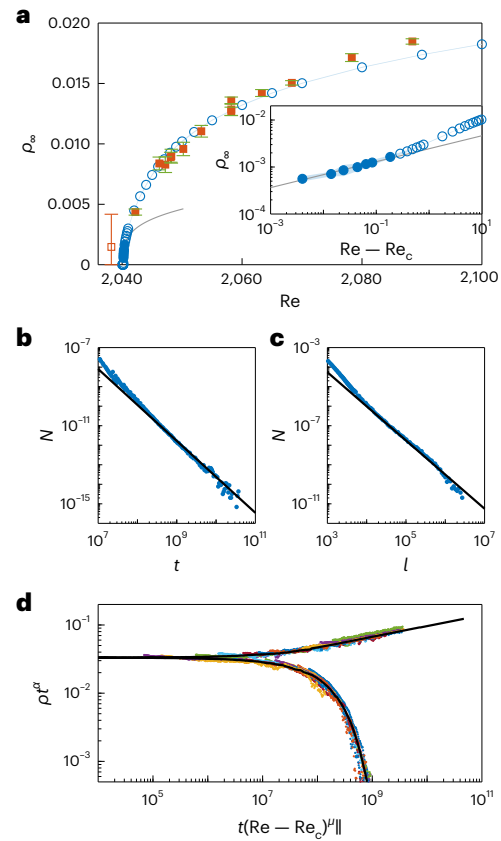


Fig. 3 | Scaling relationships obtained by simulating equation (3) using the experimentally obtained puff interactions. a, Statistical equilibrium puff density ρ_∞ as a function of Re showing the continuous transition from a laminar state to a turbulent state. Square symbols are experimental results from the quasiperiodic pipe. The open square symbol for $\text{Re} = 2,038$ represents the fact that experimental limitations make it impossible to obtain a reliable value at that Re. Inset: log–log plot of ρ_∞ versus $(\text{Re} - \text{Re}_c)$. The grey solid line is the best fit corresponding to $\rho_\infty \propto (\text{Re} - \text{Re}_c)^{\beta^{\text{DP}}}$ with $\beta^{\text{DP}} = 0.276$. Open symbols were excluded from the fit. Data are presented as mean steady-state values, and error bars are the minimum and maximum values. For the experimental data, the sample size used is seven. For the simulation, the sample size varies for each Re and is given in Supplementary Table 3. **b**, Scale-invariant laminar gap time distribution near the critical point $\text{Re} = 2,040.22$ ($\text{Re} - \text{Re}_c = 0.004$). The solid black line corresponds to the theoretical exponent $\mu_{\parallel}^{\text{DP}} = 1.841$. **c**, Scale-invariant laminar gap length distribution near the critical point $\text{Re} = 2,040.22$ ($\text{Re} - \text{Re}_c = 0.004$). The solid black line corresponds to the theoretical exponent $\mu_{\perp}^{\text{DP}} = 1.748$. **d**, Data collapse of the time-dependent turbulent fraction $\rho(t)$. Re ranges from 2,040.0 to 2,040.6. Solid black lines are universal scaling functions obtained from a bond DP simulation, and the data collapse determines the only fitting parameter, $\text{Re}_c = 2,040.216$. Here, $\alpha = \beta/\nu_{\parallel} = 0.159464$ is the $1 + 1$ -dimensional DP order parameter scaling exponent at criticality³⁶.

turbulent fluctuations within and between puffs, with an effective diffusion coefficient D_{puff} . In addition to equation (3), each puff experiences decay and splitting with rates $\tau_{d,i} = \tau_d(\text{Re}, x_i - x_{i-1})$ and $\tau_{s,i} = \tau_s(\text{Re}, x_{i+1} - x_i)$, respectively, accounting for the presence of an upstream/downstream puff as measured in the experiment. Details of their analytical expression can be found in Supplementary Information Section V.B.2.

Equation (3) was solved numerically using an explicit Euler–Maruyama scheme in an $L_x = 10^8 \cdot D$ -long domain using periodic boundary conditions. Graphics processing unit accelerated computation was used to resolve the large spatial and temporal scales at play.

For each Re investigated, the initial state was chosen to be equally spaced puffs with separation $\Delta x = 40 D$ corresponding to a quench experiment. After all transients have vanished ($t \gg 10^{10}$ for $\text{Re} \approx \text{Re}_c$;

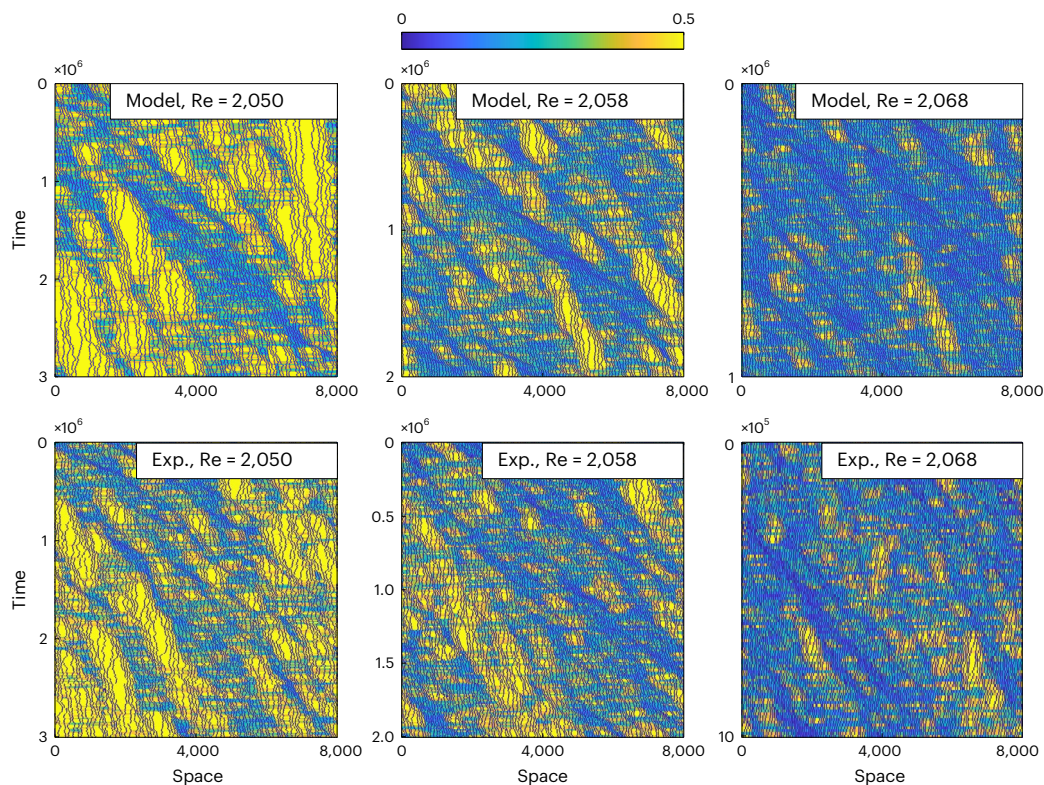


Fig. 4 | Puff jamming in pipe flow represented by a local Lindemann criterion. We define a dimensionless measure of the local fluctuations in puff spacing with the mean of the puff spacing by $\lambda = \sigma_7(\delta x)/\bar{\delta x}$, where δx is the puff spacing, σ_N is the standard deviation averaged over N neighbours, and the overbar denotes a global average. Values below 0.2 (black) represent a locally ordered phase, and

values above 0.3 (yellow) correspond to a locally disordered or fluid state. Each panel is a spatiotemporal snapshot in a comoving frame where puffs appear in black and λ is shown using the colourmap. As Re approaches the critical points, jammed crystalline regions melt away due to fluctuations. ‘Exp.’ denotes data from experiment.

see the Supplementary Information for details), the statistical equilibrium puff density ρ_∞ was measured and is presented in Fig. 3a (blue circles). The transition appears to be continuous, ruling out a first-order transition. Close to the critical point, $\rho_\infty(\text{Re})$ is well described by a power law $\rho_{\text{eq}} \propto (\text{Re} - \text{Re}_c)^\beta$, with $\text{Re}_c = 2,040.22$, where $\beta = 0.276$ is the exponent for the DP universality class (grey line in inset of Fig. 3a). Note that, as is typical for a phase transition, microscopic rules such as puff interactions (Fig. 2a), diffusion coefficient (Supplementary Fig. 12) or puff widths (Supplementary Fig. 4) do not show any sudden change near the critical point, instead showing a weak Reynolds number dependence that does not alter as we pass through the critical point.

Within the DP framework, scale-invariant patterns are expected close to the critical point, as can be seen in Fig. 1c. Quantitatively, the laminar gap distributions in both time and space are plotted in Fig. 3b,c. A power law distribution is observed, and the measured exponents are in close agreement with their DP theoretical predictions (grey lines in Fig. 3), showing that the process is scale invariant. An even more stringent test is the data collapse expected for the time-dependent turbulent fraction in the vicinity of the critical point. As shown in Fig. 3c, the data precisely fall on the universal scaling functions (black curves) predicted by DP.

The large time scales and fluctuations close to critical make it impossible experimentally to approach the scaling range for the puff density seen in Fig. 3. However, using an improved version of the setup in ref. 26, the technique described there allows us to closely approach the critical point. Exploiting the memoryless (that is, non-aging) nature of puffs, puff patterns exiting the pipe were re-created at the pipe entrance, which effectively implements periodic boundary conditions. Starting from some arbitrary sequence of puffs (corresponding to an initial puff density), the flow could be followed until it reached a steady

state with a corresponding puff density (Supplementary Information Section II). A statistically converged puff density could be obtained for Reynolds numbers as low as $\Delta\text{Re} = 2$ from the critical point. At Re closer to critical, the long time scales, increased fluctuations and stringent control on Re required (due to the steep change in puff density) make it impossible to obtain the puff densities. For instance, at $\text{Re} = 2,038$ (the data point indicated with an open symbol), even after a time of 10^9 advective time units (corresponding to a month of measurement time), the fluctuations were too large to obtain a reliable estimate of the puff density, as reflected in the large error bar. Overall, the experimentally observed patterns and the turbulent fraction (Fig. 3) are found to be in excellent agreement with the corresponding model predictions, suggesting that our model indeed includes all the essential processes and interactions of turbulent structures in the vicinity of the critical point.

Above the critical point, both experiments and simulations indicate the presence of a jammed crystalline phase, as shown in Fig. 4. In fact, at the closest Re to the critical point where converged experimental data were obtained, the jammed crystalline phase is found to persist, and consequently the experiments remain outside the scaling range. This jammed crystalline phase is present throughout the puff regime, but the fraction of jamming reduces as the Reynolds number approaches the critical point. To quantify this observation, we show in Fig. 4 a simple measure of short-range crystalline order based on the Lindemann criterion, where we compare the fluctuations in puff spacing with its mean. The melting of the jammed crystalline regions is evident as the critical point is approached. This jammed phase establishes local short-range order and is in that respect comparable to the well-known stripe patterns in planar shear flows⁵. Given that the flow reaches this jammed phase only after time scales in excess of 10^4 advective time units, it has been overlooked in earlier studies.

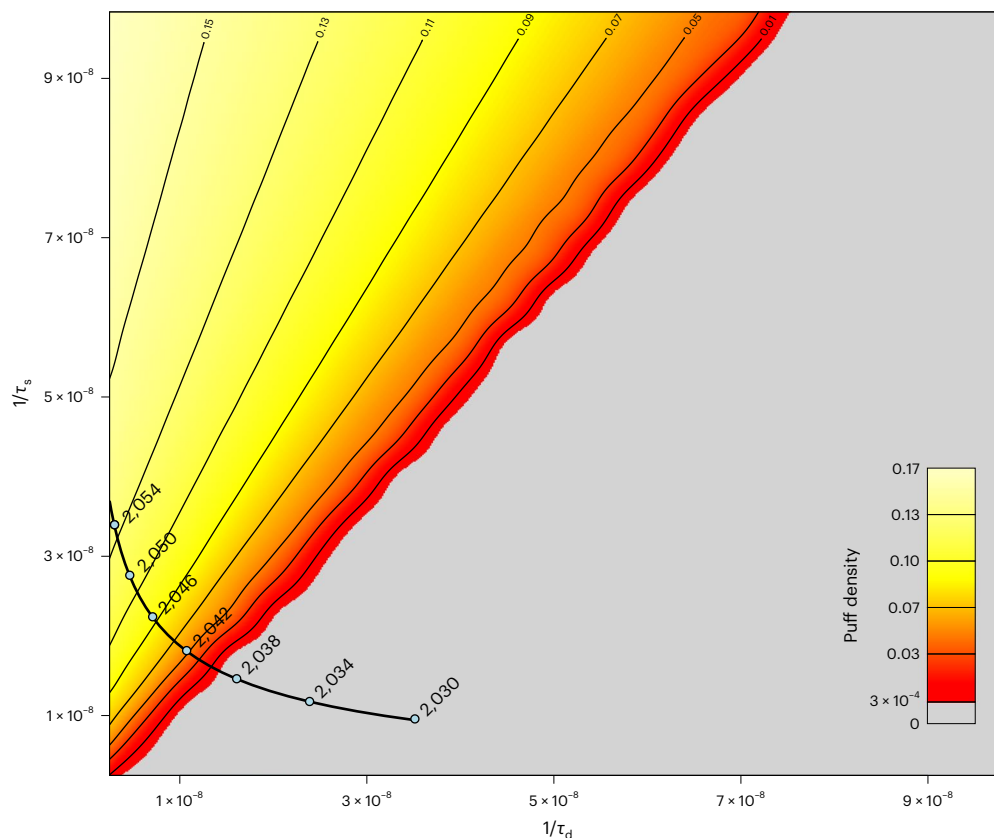


Fig. 5 | Puff density as a function of the rates at which puffs split ($1/\tau_s$) and decay ($1/\tau_d$). The experimental values of the splitting and decay rates are denoted by the Re at which they were measured and lie on the black line labelled with values of Re in the range 2,030 to 2,054.

Finally, we wanted to verify that our results are robust to variation of model parameters by exploring how the phase diagram of interacting puffs depends on individual puff splitting and decay rates. To this end, we devised a computationally efficient lattice model of the puff interaction dynamics uncovered in our experiments, closely related to the statistical hydrodynamics of equation (2) (see Supplementary Information Section V for full details). This model permits even greater scale-up than the continuous puff model and allows us to readily scan through an order of magnitude of puff splitting and decay rates. In the experiment, the values of τ_d and τ_s are given by the Reynolds number, whereas in the model, we can independently vary the two time scales and therefore more broadly test the universality of the transition in the puff density. In Fig. 5, we show the phase diagram of the puff density computed as a function of the splitting and decay lifetime. We plot the corresponding line that the experiments follow and note that we universally obtain a DP transition in this diagram whenever we cross from a low-density to a high-density puff state (from the grey area to the coloured area in the figure). Thus, we conclude that the DP transition is robust and does not depend on the precise values of the splitting and decay rates in our model.

In conclusion, we have shown that the nature of the laminar–turbulent transition in pipes can be inferred by characterizing the puff interactions experimentally and using statistical mechanics to capture the intrinsically multiscale aspect of the phenomena to predict the phase diagram and asymptotic critical phenomena (Supplementary Information Section V). Although long temporal and spatial scales have been anticipated from previous studies¹², the requirement of a system size of ($L_x = 10^8 D$) and a simulation time of 10^{12} advective time units to reach a statistical equilibrium is far beyond those found in other flows^{21,22}. To put this into perspective in the current experimental setup, a single data point well within the DP scaling range would require a measurement time of approximately 100 years and a pipe 4,000 m

long. This DP scaling regime only extends to 0.05% of the critical point; beyond this, puff interactions take over. In the resulting jammed/crystalline regime, flow patterns equilibrate several orders of magnitude faster. It is this circumstance that allows us to directly resolve turbulent fractions in experiments as close as 0.1% from critical and in doing so to validate the model predictions, albeit outside of the scaling range.

Our work extends the generality of the DP transition phenomenon to open, pressure-driven flows and identifies the extent of the critical regime beyond which specific interactions start to dominate, leading to the novel hydrodynamic behaviour of puff jamming. Our results provide a definitive resolution to a 140-year-old puzzle in pipe flow and underscore how statistical mechanics can lead to profound quantitative and predictive insights on turbulent flows and their phases.

Online content

Any methods, additional references, Nature Portfolio reporting summaries, source data, extended data, supplementary information, acknowledgements, peer review information; details of author contributions and competing interests; and statements of data and code availability are available at <https://doi.org/10.1038/s41567-024-02513-0>.

References

1. Reynolds, O. An experimental investigation of the circumstances which determine whether the motion of water shall be direct or sinuous and the law of resistance in parallel channel. *Philos. Trans. R. Soc. Lond.* **174**, 935 (1883).
2. Rotta, J. Experimenteller Beitrag zur Entstehung turbulenter Strömung im Rohr. *Ing.-Arch.* **24**, 258–281 (1956).
3. Wignanski, I. J. & Champagne, F. On transition in a pipe. Part 1. The origin of puffs and slugs and the flow in a turbulent slug. *J. Fluid Mech.* **59**, 281–335 (1973).

4. Shimizu, M. & Kida, S. A driving mechanism of a turbulent puff in pipe flow. *Fluid Dyn. Res.* **41**, 045501 (2009).
5. Tuckerman, L. S., Chantry, M. & Barkley, D. Patterns in wall-bounded shear flows. *Annu. Rev. Fluid Mech.* **52**, 343–367 (2020).
6. Avila, M., Barkley, D. & Hof, B. Transition to turbulence in pipe flow. *Annu. Rev. Fluid Mech.* **55**, 575–602 (2023).
7. Song, B. & Hof, B. Deterministic and stochastic aspects of the transition to turbulence. *J. Stat. Mech. Theory Exp.* **2014**, P02001 (2014).
8. Manneville, P. On the transition to turbulence of wall-bounded flows in general, and plane Couette flow in particular. *Eur. J. Mech. B Fluids* **49**, 345–362 (2015).
9. Barkley, D. Theoretical perspective on the route to turbulence in a pipe. *J. Fluid Mech.* **803**, P1 (2016).
10. Pomeau, Y. The long and winding road. *Nat. Phys.* **12**, 198–199 (2016).
11. Goldenfeld, N. & Shih, H.-Y. Turbulence as a problem in non-equilibrium statistical mechanics. *J. Stat. Phys.* **167**, 575–594 (2017).
12. Avila, K. et al. The onset of turbulence in pipe flow. *Science* **333**, 192–196 (2011).
13. Pomeau, Y. Front motion, metastability and subcritical bifurcations in hydrodynamics. *Physica D* **23**, 3–11 (1986).
14. Chaté, H. & Manneville, P. Transition to turbulence via spatio-temporal intermittency. *Phys. Rev. Lett.* **58**, 112 (1987).
15. Moxey, D. & Barkley, D. Distinct large-scale turbulent-laminar states in transitional pipe flow. *Proc. Natl Acad. Sci. USA* **107**, 8091–8096 (2010).
16. Sipos, M. & Goldenfeld, N. Directed percolation describes lifetime and growth of turbulent puffs and slugs. *Phys. Rev. E* **84**, 035304 (2011).
17. Barkley, D. Simplifying the complexity of pipe flow. *Phys. Rev. E* **84**, 016309 (2011).
18. Shi, L., Avila, M. & Hof, B. Scale invariance at the onset of turbulence in Couette flow. *Phys. Rev. Lett.* **110**, 204502 (2013).
19. Shih, H.-Y., Hsieh, T.-L. & Goldenfeld, N. Ecological collapse and the emergence of travelling waves at the onset of shear turbulence. *Nat. Phys.* **12**, 245 (2016).
20. Chantry, M., Tuckerman, L. S. & Barkley, D. Universal continuous transition to turbulence in a planar shear flow. *J. Fluid Mech.* **824**, R1 (2017).
21. Lemoult, G. et al. Directed percolation phase transition to sustained turbulence in couette flow. *Nat. Phys.* **12**, 254–258 (2016).
22. Klotz, L., Lemoult, G., Avila, K. & Hof, B. Phase transition to turbulence in spatially extended shear flows. *Phys. Rev. Lett.* **128**, 014502 (2022).
23. Goldenfeld, N. *Lectures on Phase Transitions and the Renormalization Group* (Addison-Wesley, 1992).
24. Dauchot, O. & Bertin, E. Subcritical transition to turbulence: what we can learn from the physics of glasses. *Phys. Rev. E* **86**, 036312 (2012).
25. Hof, B., De Lozar, A., Avila, M., Tu, X. & Schneider, T. M. Eliminating turbulence in spatially intermittent flows. *Science* **327**, 1491–1494 (2010).
26. Mukund, V. & Hof, B. The critical point of the transition to turbulence in pipe flow. *J. Fluid Mech.* **839**, 76–94 (2018).
27. Barkley, D. et al. The rise of fully turbulent flow. *Nature* **526**, 550 (2015).
28. Kreilos, T. et al. Bypass transition and spot nucleation in boundary layers. *Phys. Rev. Fluids* **1**, 043602 (2016).
29. Wang, X., Shih, H.-Y. & Goldenfeld, N. Stochastic model for quasi-one-dimensional transitional turbulence with streamwise shear interactions. *Phys. Rev. Lett.* **129**, 034501 (2022).
30. Hinrichsen, H. Non-equilibrium critical phenomena and phase transitions into absorbing states. *Adv. Phys.* **49**, 815–958 (2000).
31. Helbing, D. Traffic and related self-driven many-particle systems. *Rev. Mod. Phys.* **73**, 1067 (2001).
32. Klumpp, S. & Hwa, T. Stochasticity and traffic jams in the transcription of ribosomal RNA: Intriguing role of termination and antitermination. *Proc. Natl Acad. Sci. USA* **105**, 18159–18164 (2008).
33. Kim, S. & Jacobs-Wagner, C. Effects of mRNA degradation and site-specific transcriptional pausing on protein expression noise. *Biophys. J.* **114**, 1718–1729 (2018).
34. Chatterjee, P., Goldenfeld, N. & Kim, S. DNA supercoiling drives a transition between collective modes of gene synthesis. *Phys. Rev. Lett.* **127**, 218101 (2021).
35. Lighthill, M. J. & Whitham, G. B. On kinematic waves II. A theory of traffic flow on long crowded roads. *Proc. R. Soc. Lond. A* **229**, 317–345 (1955).
36. Jensen, I. Low-density series expansions for directed percolation on square and triangular lattices. *J. Phys. A* **29**, 7013–7040 (1996).

Publisher's note Springer Nature remains neutral with regard to jurisdictional claims in published maps and institutional affiliations.

Springer Nature or its licensor (e.g. a society or other partner) holds exclusive rights to this article under a publishing agreement with the author(s) or other rightsholder(s); author self-archiving of the accepted manuscript version of this article is solely governed by the terms of such publishing agreement and applicable law.

© The Author(s), under exclusive licence to Springer Nature Limited 2024

Methods

Methods are described in the main text and Supplementary Information.

Data availability

All experimental data presented in this article are available online in the Zenodo repository at <https://doi.org/10.5281/zenodo.10308791> (ref. 37).

Code availability

All computational data presented in this paper, the codes used to generate and process those data and the codes and scripts used to generate the figures are available online in the Zenodo repository at <https://doi.org/10.5281/zenodo.10308791> (ref. 37).

References

37. Lemoult, G. Directed percolation and puff jamming near the transition to pipe turbulence. *Zenodo* <https://doi.org/10.5281/zenodo.10308791> (2024).

Acknowledgements

We gratefully acknowledge the assistance of J. M. Lopez with DNSs at an early stage of this work. This work was partially supported by two grants from the Simons Foundation (grant nos. 662985 (N.G.) and 662960 (B.H.)) and by Ministry of Science and Technology, Taiwan (grant nos. MOST 109-2112-M-001-017-MY3 and MOST

111-2112-M-001-027-MY3 (H.-Y.S.)). Part of this work was performed using computing resources of CRIANN (Normandy, France).

Author contributions

B.H., N.G. and J.M. designed the project. B.H., G. Lemoult and V.M. performed experiments and computer simulations. H.-Y.S., G. Linga, J.M. and N.G. performed theoretical calculations and computer simulations. All authors contributed to the interpretation of the data and the writing of the paper.

Competing interests

The authors declare no competing interests.

Additional information

Supplementary information The online version contains supplementary material available at <https://doi.org/10.1038/s41567-024-02513-0>.

Correspondence and requests for materials should be addressed to Nigel Goldenfeld or Björn Hof.

Peer review information *Nature Physics* thanks Ron Shnapp and the other, anonymous, reviewer(s) for their contribution to the peer review of this work.

Reprints and permissions information is available at www.nature.com/reprints.

Directed percolation and puff jamming near the transition to pipe turbulence

In the format provided by the authors and unedited

SUPPLEMENTARY INFORMATION

Directed percolation and puff jamming near the transition to pipe turbulence

This Supplementary Information contains details of the experiments as well as theoretical and numerical calculations of models of puff interactions near the laminar-turbulent transition in pipe flow.

CONTENTS

I. Multi-scale stochastic models of transitional turbulence and puff dynamics	1
II. Experimental Setup	2
III. Puff sizes	4
IV. Puff-splitting model	5
A. Stochastic hydrodynamics for puff-splitting model	6
B. Master equation for the puff-splitting model	7
C. Universality class of the puff-splitting model	8
D. Effects of puff suppression and pushing	9
V. Numerical simulations of the puff-splitting model	9
A. Lattice model of puff dynamics	10
1. Detailed description of lattice model	10
2. Puff-pushing and suppression	10
3. Comparison to experimental values	10
4. Finite-size analysis in the lattice model	11
B. Continuum model of puff dynamics	13
1. Puff diffusion coefficient	13
2. Life and splitting times	13
3. Significance and details on errors estimation	15
VI. Data and code availability statement	17
VII. Acknowledgments	17
References	17

I. MULTI-SCALE STOCHASTIC MODELS OF TRANSITIONAL TURBULENCE AND PUFF DYNAMICS

In the model considered in the main text, the unit of turbulence is considered to be a single puff, and the model describes the interactions between puffs treated as point particles. The dynamics of these puffs is modeled by rules that encapsulate the actual hydrodynamic interactions arising from the way in which one puff influences the mean velocity profile across the pipe.

The justification for the point-puff approximation comes from experiment, direct numerical simulation (DNS) and theoretical consideration. In the main text,

we show experiments and DNS results that indicate how the puff dimensions do not change significantly as one varies the Reynolds number and passes through the transition to turbulence. This shows that the singular behavior that we report is a result of collective puff interactions over system-wide scales, reflected in diverging correlation lengths in space and time that emerge from the directed percolation (DP) picture.

This conclusion also emerges from theoretical analysis. One can start by asking what is the dynamics of turbulence in general, and in particular on scales smaller than a single puff? How can effective stochastic models on multiple scales be obtained from the Navier-Stokes equations, which capture the essential features of the laminar-turbulent transition at scales ranging from within a puff to the macroscopic scale considered in the point-puff models presented here? What, if any, is the relationship between these models and the point-puff models? Do they also exhibit the characteristics of directed percolation, as originally implied by Pomeau [1]?

These questions are distinct from the model considered here, and can be addressed by attempting to derive the effective theory for turbulence from the Navier-Stokes equation, as was done in Ref. [2]. There, numerical simulations suggested that the most singular contribution to the behavior of a single puff near the onset of turbulence arose from the interplay between two weak-modes that necessarily vanish near the transition: a collective large-scale zonal flow and small-scale turbulent anisotropy. The former mode is an emergent mean flow created (activated) by the small-scale turbulence; on the other hand, the emergent mean flow suppresses (inhibits) the small-scale turbulence. The resulting effective theory has been termed a “predator-prey” or “ecological” model of the laminar-turbulent transition [2], and is a non-equilibrium counterpart to what would be Landau theory in an equilibrium transition.

Remarkably, this ecological model turns out also to be in the universality class of directed percolation, at least asymptotically close to the transition. In order to further elucidate this finding, a mean field derivation of this single puff model from the Navier-Stokes equations has been presented [3].

The final bridge between the small-scale structure of the laminar-turbulent transition and the point-puff models presented here was the extension of the ecological model for a single puff to include streamwise shear interactions between patches of turbulence [4]. This work showed that it is possible to recapitulate the entire phase diagram of transitional pipe and quasi-one-dimensional

Taylor-Couette flow, including the transitions from puffs to weak then strong slugs as Re is increased through the transition [5, 6].

Although the methodological origin of directed percolation from this multi-scale perspective is very different from what happens in the puff-splitting model of the present paper, the puff-splitting model in the present work describes decay, merging and splitting of point particles and these dynamics are sufficient for the directed percolation universality class to emerge.

In summary, we conclude from experiment RG theory and DNS that even with strong puff-puff interactions of the suppression-pushing type, the universality class for the transition to pipe turbulence is consistent with directed percolation, and that the point-puff model used in the main text is fully justified as a description of the critical regime.

II. EXPERIMENTAL SETUP

In this section, we provide complete details of the experimental setup and measurement techniques. Setup A in Fig. S1 shows a schematic of the experiments used to measure the microscopic rules governing puff dynamics. The measurements were carried out in a $D = 4 \pm 0.01$ mm pipe of length $L/D = 1500$, made of 6 segments of precision glass tubes joined together with acrylic connectors. A few of these connectors had 0.8 mm holes (perpendicular to the pipe axis) that acted as ports for pressure measurement or to perturb the flow. Puffs can be easily identified by a sharp increase in pressure drop across the pipe and by monitoring the number of puffs at different positions along the pipe, we can monitor puff decays and splittings. To avoid any consequent changes in the flow-rate and hence Re , the flow was driven in a constant mass flux mode using a metering pump from Fuji Techno Industries Corporation (model HYS A 12). This pump features three pistons operating 180° out of phase, driven by a precision servo motor ensuring a pulsation free and accurate flow rate (better than 0.1%) over the entire operating range. The temperature of the fluid, distilled water, was measured by platinum RTD probes at the inlet and outlet of the pipe. The fluid viscosity was calculated from a fit to standard temperature-viscosity data. The fluid temperature was maintained constant and equal to $22 \pm 0.05^\circ C$ by means of a heat exchanger resulting in an estimated variation of ± 5 in terms of Re over several days. The flow is perturbed $150D$ downstream of the inlet and the laminar profile can be considered fully developed. The laminar flow is then disturbed by simultaneously injecting and withdrawing fluid by a push-pull perturbation via two 0.8 mm diametrically opposed holes in one of the acrylic connectors. As illustrated by Fig. S1, the perturbation mechanism consists of a coil to move a small magnetic cylinder, which injects water from one of the ports, while simultaneously withdrawing it from the other port, thus ensuring a disturbance with zero net

flux. It is known (see, for example, [7]) that provided a perturbation is successful in creating turbulence, the resulting puff is independent of the perturbation details and all puffs are statistically identical, with a fixed average length at a given Re . The state of the flow is monitored by measuring the differential pressure drop across a distance of $3D$, using variable-reluctance differential pressure sensors from Validyne (model DP-45). As a puff passes the pressure ports, the increased skin friction results in an increased differential pressure across the pair of pressure ports. Thus, the passage of a puff across the measurement point shows up as a peak in the pressure signal at that time instant as seen in Fig. S2a, which shows the signal corresponding to a train of puffs.

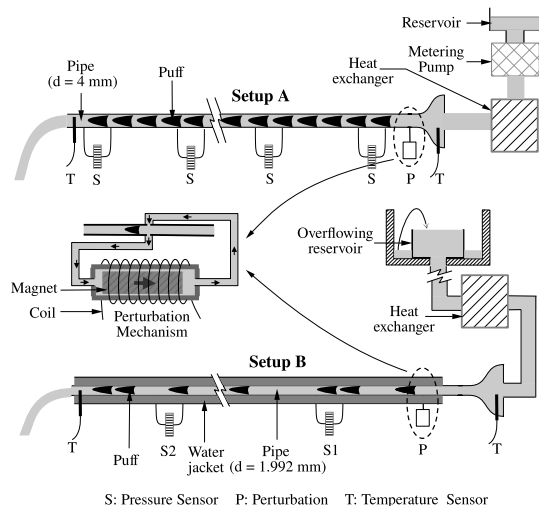


FIG. S1 A schematic of the experimental set-ups and the perturbation mechanism used to trigger puffs. Setup A was used to measure the microscopic rules governing puff motion and interactions. Setup B, is the quasi-periodic pipe used to obtain the steady state characteristics for different Re .

To quantify the inter-puff repulsion, two kinds of measurements were carried out, with the pressure signals being monitored $75D$ and $425D$ downstream of the perturbation. In the first series of measurements, two puffs were generated close to one another, at various separations. The pressure traces were used to determine the time at which the puffs passed each of the measurement points. This could be used to determine the mean speed of each puff as well as their relative speed. These measurements reveal that the speed of the downstream puff is affected by the upstream one and depends on their separation. However the speed of the puff that is upstream is unaffected and it has the same speed as an isolated puff, with its Re dependence matching the results of [5]. In the second type of measurement, a train of 100 equally spaced puffs is generated and measuring the time delays between each of the peaks in the pressure signal (corresponding to puffs) yields the speed of each of the puffs. Due to the repulsion, the first few puffs do spread out by the time they reach the second sensor and are ignored for

further processing, but the inter-puff distance of all the other puffs is maintained. The experiment is repeated 10 times for the same inter-puff spacing and the velocity is averaged over all the puffs to obtain a mean speed. As each puff in the train has a puff upstream, their speed is different from that of an isolated puff. The speed of a puff as a function of distance from an upstream one can be obtained by repeating this experiment for different inter-puff spacings.

As a further check, this information can be used to calculate the increase in relative separation between puffs that are initially closely spaced, and the results are in good agreement with the earlier measurements involving only 2 puffs.

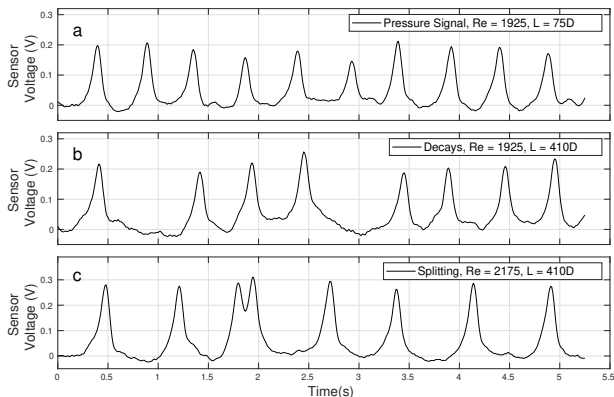


FIG. S2 (a) A typical pressure trace from the sensor at $75D$ for a puff train with an inter-puff spacing of $60D$, at $Re = 1925$. (b) The same puff train at $410D$ showing two decays, identifiable by the larger spacing at two locations, as compared to the signal at $60D$ above. (c) A puff train with an inter-puff spacing of $100D$ at $Re = 2175$ showing a smaller than typical spacing at one location, indicating a puff splitting.

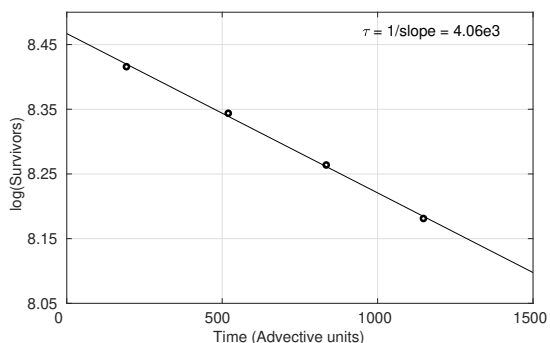


FIG. S3 A straight line fit of the logarithm of survivors (puffs that have survived without decaying) at different times (obtained from the 4 measurement locations), showing an exponential decay of survivors. The inverse of the slope is the time-scale of decay. The figure is obtained from measurements at $Re = 1925$ and an inter-puff spacing of $60D$, some pressure traces of which are shown in Fig.S2(a) and (b).

To determine the dependence of inter-puff spacing on

decay and splitting lifetimes, the same set-up was used, but with 4 sensors at $75D$, $410D$, $73D$ and $1055D$ downstream of the perturbation point. A train of equally spaced puffs with a specific spacing was generated and the pressure traces recorded at each sensor. As mentioned previously, except for the first few puffs, the train travelled downstream while maintaining the inter-puff spacing, unless a splitting or decay occurred. Indeed, decays and splittings were identified by significantly larger or smaller gaps between adjacent puffs than the initially chosen spacing. Examples of typical pressure traces are shown in Fig. S2. Fig. S2(a) shows a portion of the puff train consisting of 10 puffs with an inter-puff spacing of $60D$ at $Re = 1925$, recorded at the first pressure sensor, located just downstream ($75D$) of the perturbation. Fig. S2(b) shows the same portion of the train at the next sensor, located $410D$ downstream of the perturbation point. Two decays can be identified due to the larger spacing as compared to the original train. Similarly, Fig. S2c shows the pressure trace at the same sensor, but at $Re = 2175$, for an initial inter-puff spacing of $100D$, where one splitting event can be identified due to a smaller inter-puff spacing than originally chosen. Thus, for a given puff train, the number of decays or splittings at each sensor can be determined. In practice, due to the faster than exponential decrease (increase) in decay (splitting rates), there are practically only decays for $Re < 2030$ and only splittings for $Re > 2050$, and hence it suffices to count the number of puffs at each sensor location to determine the number of decays (or splittings) at each sensor.

With this information, the fraction that survive without a decay or split can be plotted as a function of time (equivalent to downstream location as the puffs advect downstream at a well defined average speed). This reveals an exponentially decaying or memoryless distribution of the survivors allowing us to extract a time-scale from a fit. Note that this is a slight modification of a technique to obtain lifetimes that has become standard for pipe flow; see, for example, [8]. Fig. S3 shows the survivor distribution for $Re = 1925$ and an inter-puff spacing of 60 , corresponding to the measurements whose pressure traces are shown in Fig. S2a and b. These measurements are repeated for different Re and inter-puff spacings to yield characteristic decay and splitting times as a function of both puff spacing and Re .

Finally, by looking at the distribution of arrival times of 1000 isolated puffs at these 4 locations, the diffusive nature of the puff propagation was shown and the diffusive coefficient calculated as a function of Re .

The long time-scale experiments to experimentally obtain the steady-state turbulent fraction as a function of Re require a much bigger system size and a tighter control on Re for long periods of time. As measurements were carried out closer to critical as compared to [7], the setup here is a modified version of the one used in that study, resulting in a tighter control of Re and temperature. A schematic of the set-up is shown as setup B

in Fig. S1. The pipe had a nominal inner diameter of $D = 2\text{mm}$ and a total length of 18 meters, or $9000D$. However a determination of the diameter by measuring the pressure drop across a section of the pipe using a precision, piezo-resistive, differential pressure sensor (model PN1M from Sensors) gave a value of 1.992 mm and this value is what is used in calculating Re . As before, this consisted of glass pipe-sections joined together with custom made acrylic connectors, some of which had ports for perturbing the flow or measurement of pressure. The pipe is gravity-driven, with the working fluid, de-ionized water, being supplied from reservoir that is more than 20 meters above the pipe. The reservoir is continuously overflowing, which ensures a precise pressure-head that drives the flow. The reservoir is mounted on motorized, vertical guide-rails, permitting fine adjustments to the height of the reservoir, and hence the flow rate and Re . The convergent section through which the water enters the pipe and the precise machining of the connectors ensures that the pipe remains laminar up to $Re \approx 5000$, which is far above the Re range studied.

The flow-rate is continuously measured to an accuracy of better than 0.05% by collecting the water exiting the pipe for a fixed amount of time and weighing it with a precision electronic scale. RTD platinum probes were used to measure the temperature at the inlet and exit of the pipe. A little before entering the pipe, the water passes through a heat exchanger, with an associated temperature controller. As shown in the schematic, there is an acrylic pipe with an diameter of 50 mm, that is coaxial to the 2 mm measurement pipe and surrounds it. Water, whose temperature is regulated by a temperature-controller is circulated in the annular space between these pipes which acts as a water jacket to regulate temperature variations of the measurement pipe. To allow a better control, the outer pipe is heat-insulated by covering it with standard pipe insulation. The two temperature controllers (one for the working fluid and the other for the water jacket) are used in a feedback loop with a target of maintaining a zero temperature difference between inlet and outlet of the the measurement pipe and a desired value (usually 20° at the inlet. Both targets are achieved to better than $\pm 0.01^\circ$ for as long as desired. The temperature of the working fluid is taken to be the mean of the temperatures at the two ends of the pipe. As with the earlier constant flux set-up, the viscosity of the water is determined by a fit to standard data. With this viscosity and the measured flow-rate, the Re is calculated. Experiments to measure the turbulent fraction close to the critical point can take anywhere between several hours to several weeks and it is important to maintain the Re for such extended periods of time. In the course of the experiment, the Re can change due to two reasons. One is the temperature associated viscosity change, with a change of 0.01° resulting in a change of around 1 in Re . Another is the change in frictional drag due a change in the number of puffs in the pipe due to splitting or decay, with one extra puff causing a decrease of around 1 in Re .

A feedback loop counters any such deviation from the set Re by an adjustment of the vertical position of the reservoir and hence the flow-rate, in order to bring back the Re to the set value. With this method, a long term stability of the Re to better than ± 1 can be achieved.

The flow is perturbed $150D$ from entrance using the same push-pull perturbation described earlier for the pump driven set-up and shown in the schematic of the perturbation mechanism in Fig.S1. The puffs are monitored near the pipe entrance and exit using DP-45 variable-reluctance differential pressure sensors from Validyne, which measure the pressure across $8D$. Specifically, the locations are $245D$ and $8495D$ downstream of the perturbation point, and are indicated in the schematic by points S1 and S2 respectively

The procedure to determine the steady-state turbulent fraction is as follows. A number of puffs, typically uniformly spaced, are generated using the perturbation and serve as the initial condition. These puffs advect downstream. As each of them passes the pressure measurement location S2, a peak is detected in the pressure signal. This peak detection automatically triggers the perturbation to generate a new puff near the inlet. Shortly thereafter, the newly generated puff passes point P1, generating a peak in the pressure signal which confirms that it was successfully generated. Thus, the pattern of puffs passing the point P2 and exiting the pipe is generated at the pipe inlet and verified at point S1. As puffs are statistically identical, this procedure should not change the statistical evolution of the flow. In this way, the evolution of turbulence can be followed for long periods of time till it reaches a steady-state. In this paper, we use the puff density (number of puffs per unit length) as a proxy for the turbulent fraction as the former quantity is well defined while the latter one depends on the cut-off chosen for differentiating laminar from turbulent flow. The mean puff density at a given Re is calculated by simply counting the number of puffs in one period and then averaging over long times in the steady state.

III. PUFF SIZES

In the main paper, we point out that, as is typical of a phase transition, the microscopic rules such as puff interactions or the diffusion coefficient but vary smoothly as we pass the critical point and do not exhibit any sudden change there. Here, we present additional evidence to strengthen this claim by looking at typical puff widths at different Re . Well separated (non-interacting) puffs were triggered and the pressure signal recorded further downstream. The pressure signals for 10 puffs were phase averaged (by using the peak of the pressure signal as a reference point), yielding an ensemble-averaged pressure signal. This was repeated at several Re below and above critical and the results are shown in Fig. S4. The width of the pressure peak is a measure of the puff width, and

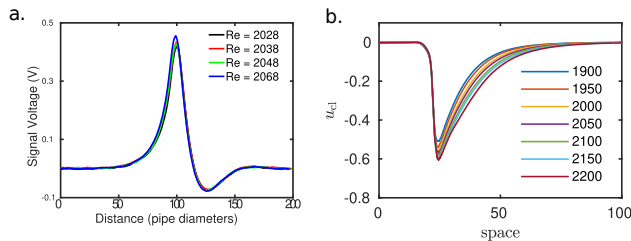


FIG. S4 Profile of a single puff as a function of Re , showing puff widths at various Re straddling the critical point, showing that the puff sizes change slowly and smoothly with Re . (a) Experimental voltage signal from a pressure sensor (b) Centreline velocities obtained from DNS

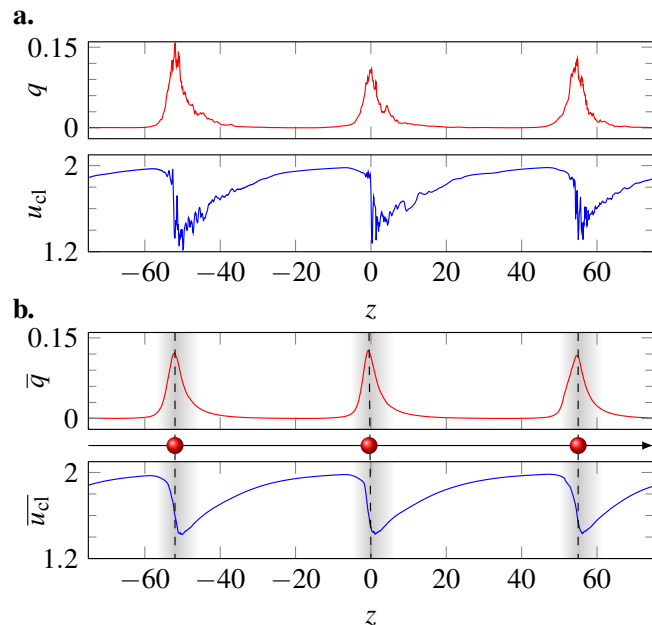


FIG. S5 a. Instantaneous turbulent kinetic energy of the perturbation averaged over cross-section of the pipe $q(z, t) = \int (\mathbf{u} - \mathbf{u}_{\text{lam}})^2 d^2\mathbf{r}$ and the streamwise centerline velocity u_{cl} from a direct numerical simulation showing three interacting turbulent puffs. \mathbf{u} is the velocity field, \mathbf{u}_{lam} is the laminar velocity field. **b.** Time averaged, in a co-moving frame, q and u_{cl} for the same simulation. While each puff is unique due to a fully 3d and temporal dynamics (a), their time-averaged counterpart are statistically equivalent (b). The spatially localized turbulent kinetic energy justifies the point-like particle approach and the long tail of the centerline velocity perturbation provides an insight into the origin of their interactions.

as is clear, this does not change appreciably with Re as we pass through the critical point.

IV. PUFF-SPLITTING MODEL

In this chapter of the Supplementary Information, we develop a theoretical description of the statistical me-

chanics of puffs near the critical Reynolds number. We start with a description of turbulent puffs in a pipe that is coarse-grained so that each puff is considered to be a single particle that can move on a line or a one-dimensional (1D) lattice. The turbulent puffs can spontaneously relaminarize (i.e. “die”), diffuse and split (i.e. “birth”). A general configuration will be a gas of puffs that is very dilute near the laminar-turbulence transition, and becomes increasingly dense as the Reynolds number is increased. We wish to understand the functional form of this mean density field, which we will sometimes call the turbulent fraction. In addition to their intrinsic dynamics, puffs are being advected downstream by the mean flow, which we will take to be moving from left to right.

Systems of particles hopping predominantly in one direction along a line, with strong repulsive interactions, arise in many fields of physics, and are generally described by a class of models known as asymmetric exclusion processes (ASEP) [9, 10]. The variant of these models that is appropriate here as a minimal model is based upon the totally asymmetric exclusion process (TASEP), in which only unidirectional hopping is allowed. The question that is usually asked of ASEP models is how is the bulk dynamics of the particles affected by the boundary conditions? In these models, particles are injected at a given rate on the left and removed with a given rate on the right of the system. In our case we are primarily interested in the case of periodic boundary conditions. Particles are, however, not conserved in our case: they are born through splitting, and they die through decay. Thus the appropriate model for puffs combines TASEP with the additional birth and death processes of DP.

Let n_i be the occupation number of the site i in a 1D periodic lattice of N sites. Then the puff-splitting model (ignoring for now puff-puff interactions) is given by the following stochastic processes:

1. Puff at site i is removed with rate ω_d (*decay*)
2. Puff at site i moves to site $i+1$, if that site is empty, with rate p (*propagation*)
3. Puff at site i creates a puff at site $i+1$, if that site is empty, with rate ω_s (*splitting*)

To implement this model, random asynchronous updating should be used, in which the three rate processes are carried out on randomly chosen particles in random order, with probabilities per unit time given by the coefficients p , ω_d and ω_s .

The mean field equation for this process is given by

$$\partial_t \langle n_i \rangle = -p \langle n_i (1 - n_{i+1}) \rangle + p \langle n_{i-1} (1 - n_i) \rangle - \omega_d \langle n_i \rangle + \omega_s \langle n_{i-1} (1 - n_i) \rangle \quad (\text{S1})$$

The first term describes the process in which a puff hops away from site i onto the neighbouring downstream site $i+1$, but only if the destination site is empty. This

process happens with a rate p . If the puff does not hop, it is effectively moving backwards (i.e. upstream) compared to the mean flow of the puffs. The second process is similar but is a flow onto site i from the upstream site $i - 1$. Together these terms represent single puff hopping unless blocked by a downstream puff. The third term represents decay, and the fourth term puff-splitting. Note that this term resembles the second half of the puff hopping process, but its effect is different because there is no term which effectively removes the puff at site i , as does the first term in equation (S1).

Living in one dimension, puff-puff interactions are very strong, and there are two additional microscopic interactions that need to be considered in addition to the fact the puffs cannot pass through one another: a puff that is upstream of another occupying its nearest-neighbour site can neither split nor hop to the right, until the downstream puff has itself hopped downstream or decayed. First, the lifetime of the puff that is downstream of its nearest-neighbour will have a drastically shortened lifetime (by perhaps 5 orders of magnitude) compared to a free puff. We will call this ‘‘suppression’’; it arises from the way in which a puff distorts the mean velocity profile. Second, the puffs have a strong short-range repulsion, which we will call ‘‘pushing’’: a puff that is created by splitting will for a short distance experience a faster downstream velocity that has the effect of separating it quickly from its mother puff. If the daughter does not get pushed then it will have a high likelihood of decaying rapidly.

These interactions can be added to the simple puff-splitting model by two additional rules. *Suppression* can be modeled by assuming that the decay rate is much greater if a puff is immediately downstream of another puff, i.e. $\omega_d \rightarrow \tilde{\omega}$. *Pushing* can be modeled by introducing an increased hopping rate \tilde{p} if a puff is immediately downstream of another puff, i.e. $p \rightarrow r$. For now, we will not include these terms.

If we set $p = 0$, then this model describes purely splitting and decay. Since splitting followed by decay represents hopping (i.e. anisotropic diffusion), and there is a limit of one puff per site, this model includes the four basic processes of directed percolation (DP): diffusion, de-coagulation, coagulation and annihilation [11]. For ω_d large enough, the ultimate fate of the system is to be empty. As ω_d becomes smaller, there will be a continuous transition in the DP universality class to a state with persistent mean number of particles $\rho \equiv \langle n_i \rangle \sim (\omega_c - \omega_d)^\beta$, with $\beta = 0.276$ in 1D.

The question that we now address is how the additional terms in the puff-splitting model modify the critical behavior from DP. We will answer the question by writing down a stochastic hydrodynamic model for the puff-splitting model, and then analyze its critical behaviour using renormalization group arguments.

A. Stochastic hydrodynamics for puff-splitting model

The discrete stochastic puff-splitting model can be expressed as a field theory using standard techniques that

use the Doi formalism [12], followed by a Martin–Siggia–Rose [13–15] transformation to a coherent state path integral [16]. We will not use that method here, although we will need to use the result later. An alternative, shown in the next Section, is to derive the stochastic equation by writing down the master equation, and then performing a Kramers–Moyal expansion to second order to derive the corresponding Fokker–Planck equation, and thence the Langevin equation [17]. In this coarse-grained formulation that neglects higher order derivatives, the lattice becomes a continuum ($i \rightarrow x$). This amounts to writing $n_i \rightarrow \rho(x)$ and

$$n_{i+1} \approx \rho(x) + \partial_x \rho(x) + \frac{1}{2} \partial_x^2 \rho(x) \quad (\text{S2})$$

and reading off the noise, to obtain

$$\begin{aligned} \partial_t \rho = & -\omega_d \rho + \frac{1}{2} (p + \omega_s) \partial_x^2 \rho - (p + \omega_s) \partial_x \rho + \omega_s \rho (1 - \rho) \\ & + (2p + \omega_s) \rho \partial_x \rho - \frac{\omega_s}{2} \rho \partial_x^2 \rho + \sqrt{\rho(1 - \rho)} \eta \end{aligned} \quad (\text{S3})$$

where $\eta(x, t)$ is a white noise delta-correlated in space and time. The dynamics is controlled by multiplicative noise, which has the effect that the empty state is absorbing. This form of the noise arises because of the rule that there can only be one particle per site. If this were enforced by an explicit coagulation term of the form $2n_i \rightarrow n_i + \emptyset$, the equations would be the same but the minus sign in the noise term would be replaced by a plus sign.

Equation (S3) is similar to the Langevin equation for DP, but with the addition of three terms: the term proportional to $\partial_x \rho$ and the last two terms of second order in ρ . The linear term arises because the puff dynamics is diffusive (the second order term, linear in ρ) but in a frame moving with the net velocity of the puffs. This anisotropic diffusion can be removed by a Galilean transformation into the comoving frame. The second term is proportional to $\rho \partial_x \rho$ and has the functional form of the advective nonlinearity in Burgers equation. Such terms naturally arise in TASEP models, and loosely speaking lead to shocks that model the bunching up of particles, as occurs in traffic jams, transcription by ribosomes moving on mRNA etc. These shocks are regularized by the higher order derivative terms, including the third extra term and the linear diffusive term. We refer to the terms $\rho \partial_x \rho$ and $\rho \partial_x^2 \rho$ as Burgers-like terms. We will refer to the terms $\rho \partial_x \rho$ and $\rho \partial_x^2 \rho$ as Burgers-like terms, because they are of the form density multiplying a derivative of the density.

B. Master equation for the puff-splitting model

In this Section, we derive equation (S3). The puff splitting model is based on the reactions of decay, hopping and splitting process in one dimension:



where A_i denotes a particle at site i , E_i represents the vacancy at site i , and $i = 1, 2, \dots, L$. We introduce the coarse-grained particle density centered at site i over a length scale of K lattice sites with a uniform kernel as n_i , specifically,

$$n_i = \frac{1}{K} \sum_{j=-K/2}^{K/2} N_{i+j}, \quad (\text{S7})$$

where $N_i = 0, 1$ is the particle number at each site i . We denote the state vector by $\mathbf{n} = (n_1, n_2, \dots, n_L)^T$ and define the lattice density operator \mathcal{E}_i^\pm as

$$\mathcal{E}_i^\pm f(n_i) = f(n_i \pm \Delta), \quad (\text{S8})$$

and the master equation can be represented as

$$\partial_t P(\mathbf{n}, t) = \frac{1}{\Delta} \sum_i \left[(\mathcal{E}_i - 1) \omega_d n_i + (\mathcal{E}_{i-1} \mathcal{E}_i^{-1} - 1) \omega_s n_{i-1} (1 - n_i) + (\mathcal{E}_{i-1} \mathcal{E}_i^{-1} - 1) p n_{i-1} (1 - n_i) \right] P(\mathbf{n}, t), \quad (\text{S9})$$

where $\Delta = 1/K$. By applying Kramers-Moyal expansion with truncation to the second order,

$$\mathcal{E}_i^\pm \approx 1 \pm \Delta \partial_{n_i} + \frac{1}{2} \Delta^2 \partial_{n_i}^2 + \dots, \quad (\text{S10})$$

equation (S9) can be rewritten into a Fokker-Planck equation:

$$\partial_t P(\mathbf{n}, t) = - \sum_i \frac{\partial (A_i P)}{\partial n_i} + \frac{1}{2} \Delta \sum_{i,j} \frac{\partial^2 (B_{ij} P)}{\partial n_i \partial n_j}, \quad (\text{S11})$$

where

$$A_i = -\omega_d n_i - p n_i (1 - n_{i+1}) + (p + \omega_s) n_{i-1} (1 - n_i), \quad (\text{S12})$$

$$B_{ij} = [\omega_d n_i + \omega_s n_i (1 - n_{i+1}) + p n_i (1 - n_{i+1}) + p n_{i-1} (1 - n_i)] \delta_{ij} + 2p n_i (1 - n_j) \delta_{j,i+1}. \quad (\text{S13})$$

The corresponding Langevin equation in Ito's sense is

$$\partial_t \mathbf{n} = \mathbf{A}(\mathbf{n}) + \boldsymbol{\xi}(t), \quad (\text{S14})$$

$$\langle \xi_i(t) \xi_{i'}(t') \rangle = \Delta B_{ii'} \delta(t - t'). \quad (\text{S15})$$

In the continuum limit in space, the density operator is defined as

$$\tilde{\mathcal{E}}_x^\pm f[\rho(y)] = f[\rho(y) \pm \Delta \delta(y - x)], \quad (\text{S16})$$

and equation (S9) becomes

$$\begin{aligned} \partial_t P(\rho, t) = \frac{1}{\Delta} \left\{ \int (\tilde{\mathcal{E}}_x - 1) \omega_d \rho(x) P dx \right. \\ + \iint (\tilde{\mathcal{E}}_y \tilde{\mathcal{E}}_x^{-1} - 1) p \rho(y) [1 - \rho(x)] \delta(x - y - \epsilon) P dx dy \\ \left. + \iint (\tilde{\mathcal{E}}_x^{-1} - 1) \omega_s \rho(y) [1 - \rho(x)] \delta(x - y - \epsilon) P dx dy \right\}, \quad (\text{S17}) \end{aligned}$$

where ϵ is the lattice spacing.

The Kramers-Moyal expansion gives

$$\tilde{\mathcal{E}}_x^\pm \approx 1 \pm \Delta \frac{\delta}{\delta \rho(x)} + \frac{1}{2} \Delta^2 \frac{\delta^2}{\delta \rho(x)^2} + \dots, \quad (\text{S18})$$

and with truncation to the second order, equation (S17) becomes

$$\begin{aligned} \partial_t P(\rho, t) &\approx - \int \frac{\delta}{\delta \rho(x)} \{ -\omega_d \rho(x - \epsilon) + (p + \omega_s) \rho(x - \epsilon) [1 - \rho(x)] - p \rho(x) [1 - \rho(x + \epsilon)] \} dx \\ &+ \Delta \int \frac{\delta^2}{\delta \rho(x)^2} \{ \omega_d \rho(x) + (p + \omega_s) \rho(x - \epsilon) [1 - \rho(x)] + p \rho(x) [1 - \rho(x + \epsilon)] \} dx \\ &+ \Delta \iint \frac{\delta^2}{\delta \rho(x) \delta \rho(y)} \{ -2p \rho(y) [1 - \rho(x)] \delta(x - y + \epsilon) \} dx dy. \end{aligned} \quad (\text{S19})$$

By using

$$\rho(x \pm \epsilon) \approx \rho(x) \pm \epsilon \partial_x \rho(x) + \frac{1}{2} \epsilon^2 \partial_x^2 \rho(x) + \dots, \quad (\text{S20})$$

equation (S19) can be written into a Fokker-Planck equation:

$$\partial_t P(\rho, t) \approx - \int \frac{\delta}{\delta \rho(x)} [\mathcal{A}(\rho, x) P] dx + \frac{1}{2} \Delta \iint \frac{\delta^2}{\delta \rho(x) \delta \rho(y)} [\mathcal{B}(\rho, x, y) P] dx dy, \quad (\text{S21})$$

where

$$\begin{aligned} \mathcal{A}(\rho, x) &= -\omega_d \rho(x) + \omega_s \rho(x) [1 - \rho(x)] + \frac{1}{2} \epsilon^2 (p + \omega_s) \partial_x^2 \rho(x) \\ &\quad - \epsilon (p + \omega_s) \partial_x \rho(x) + \epsilon (2p + \omega_s) \rho(x) \partial_x \rho(x) - \frac{1}{2} \epsilon^2 \omega_s \rho(x) \partial_x^2 \rho(x), \end{aligned} \quad (\text{S22})$$

$$\begin{aligned} \mathcal{B}(\rho, x, y) &= \left\{ \omega_d \rho(x) + (2p + \omega_s) \rho(x) [1 - \rho(x)] + \frac{1}{2} \epsilon^2 (p + \omega_s) \partial_x^2 \rho(x) \right. \\ &\quad \left. - \epsilon (p + \omega_s) \partial_x \rho(x) + \epsilon \omega_s \rho(x) \partial_x \rho(x) - \frac{1}{2} \epsilon^2 (2p + \omega_s) \rho(x) \partial_x^2 \rho(x) \right\} \delta(x - y) \\ &\quad - 2p \left\{ \rho(x) [1 - \rho(x)] + [1 - \rho(x)] \left[-\epsilon \partial_x \rho(x) + \frac{1}{2} \epsilon^2 \partial_x^2 \rho(x) \right] \right\} \delta(x - y + \epsilon). \end{aligned} \quad (\text{S23})$$

The corresponding Langevin equation in Ito's sense is

$$\partial_t \rho(x) = \mathcal{A}(\rho, x) + \xi(x, t), \quad (\text{S24})$$

$$\langle \xi(x, t) \xi(y, t') \rangle = \Delta \mathcal{B}(\rho, x, y) \delta(t - t'). \quad (\text{S25})$$

By setting $\epsilon = 1$, near transition $\rho \ll 1$, one obtains

$$\begin{aligned} \partial_t \rho &\approx -\omega_d \rho + \omega_s \rho (1 - \rho) + \frac{1}{2} (p + \omega_s) \partial_x^2 \rho - (p + \omega_s) \partial_x \rho \\ &\quad + (2p + \omega_s) \rho \partial_x \rho - \frac{1}{2} \omega_s \rho \partial_x^2 \rho + \sqrt{a\rho - b\rho^2} \eta, \end{aligned} \quad (\text{S26})$$

where $\eta(x, t)$ is a Gaussian white noise and a and b are functions of ω_d, ω_s and p . The nonlinear term in the square root that multiplies the white noise η can be replaced by $\sqrt{\rho}$ near the transition where $\rho \rightarrow 0$. This equation is of the form of equation (S3).

C. Universality class of the puff-splitting model

The puff-splitting model without the Burgers-like terms is in the universality class of DP. We now examine whether or not the Burgers-like terms change the universality class, by calculating whether or not they are relevant or irrelevant in the renormalization group sense at the fixed point that controls DP. To do that, we will

use the field theoretic RG, in which the critical dynamics of DP is generated by a Martin-Siggia-Rose action of the form [16]

$$\begin{aligned} A(\rho, \tilde{\rho}) &= \int d^d x dt [\tilde{\rho} (\partial_t + D(r - \partial_x^2)) \rho \\ &\quad - u_3 \tilde{\rho} (\rho - \tilde{\rho}) \rho + u_4 \tilde{\rho}^2 \rho^2 + O(\rho^5)] \end{aligned} \quad (\text{S27})$$

where $\tilde{\rho}$ is a so-called response field that arises during the representation of the problem as a field theory, u_3 and u_4 are coupling constants of cubic and quartic terms, D is an effective diffusion coefficient, and r is a control parameter that vanishes at the critical point (for an excellent review, see Ref. [16], pp. 173-174). The requirement that the action be dimensionless implies that the dimensions of the fields can be expressed in terms of the momentum cut-off μ as follows: $[x] = \mu^{-1}$, $[t] = \mu^{-2}$, $[\rho] = \mu^{d/2}$, $[D] = \mu^0$, $[r] = \mu^2$, $[u_3] = \mu^{2-d/2}$, $[u_4] = \mu^{2-d}$.

The lowest order nonlinearity beyond free field theory is the cubic term, whose scaling dimension is $2 - d/2$, implying that the critical behavior deviates from mean field theory for $d < 4$ (for an introduction to the renormalization group for DP, see Ref. [16], p. 404 et seq.). The cubic nonlinearity is the only contributor to the non-analytic scaling behavior below four dimensions, and the critical behavior can be calculated using (e.g. an expansion in $4 - \epsilon$ dimensions) (see (e.g.) [18]). The quartic coupling constant u_4 has scaling dimension $2 - d$, so as the momentum cut-off $\mu \rightarrow \infty$, the quartic coupling gets weaker and weaker, and is irrelevant in the RG sense at the four dimensional fixed point that controls the behavior for $d < 4$. Thus, even as low as $d = 1$, DP is controlled by the cubic nonlinearity only. We now apply the same reasoning to the Burgers-like terms in equation (S3), but work directly with the stochastic differential equation rather than the field theoretic action.

The stochastic differential equation corresponding to the DP action of equation (S27) is [16]:

$$\partial_t \rho = -D(r - \partial_x^2)\rho - u_3 \rho^2 + \xi \quad (\text{S28})$$

$$\langle \xi(x, t)\xi(x', t') \rangle = 2u_3 \rho(x, t)\delta(x - x')\delta(t - t') \quad (\text{S29})$$

Note that the dimension of all the terms in the equation is $\mu^{2+d/2}$. Thus, to see how the Burgers-like terms scale under renormalization, we calculate the coupling constant dimensions using the known scaling dimensions of space and the field ρ . Denoting the coupling constant of the Burgers term as λ_1 , we equate

$$[\lambda_1 \rho \partial_x \rho] = \mu^{2+d/2} \quad (\text{S30})$$

to obtain

$$[\lambda_1] = \mu^{1-d/2} \quad (\text{S31})$$

At the fixed point in $d = 4$, this has negative scaling dimensions and flows to zero as $\mu \rightarrow \infty$. We conclude that this Burgers-like term is irrelevant for DP. Similarly, the coupling constant λ_2 for the Burgers-like term $\rho \partial_x^2 \rho$ scales as $\mu^{-d/2}$ and thus is also irrelevant at the DP fixed point. These results are consistent with earlier studies briefly mentioned in Ref. ([19]) (p. 471 and 477).

D. Effects of puff suppression and pushing

The experiments suggest that puffs that are close and downstream of another puff, experience an additional

rate of decay, $\tilde{\omega}$ and a higher velocity to the right. We can model suppression in the stochastic hydrodynamic model by a term that in mean field theory follows:

$$\partial_t \langle n_i \rangle = -\tilde{\omega} \langle n_{i-1} n_i \rangle \quad (\text{S32})$$

and model pushing by an enhanced hopping at a rate r for nearest neighbour downstream puffs:

$$\partial_t \langle n_i \rangle = -r \langle n_i n_{i-1} (1 - n_{i+1}) \rangle + r \langle (1 - n_i) n_{i-1} n_{i-2} \rangle. \quad (\text{S33})$$

Going to the continuum stochastic hydrodynamical description, these terms will all be represented by high order operators of the form

$$I_{\alpha\beta\gamma} \equiv \lambda_{\alpha\beta\gamma} \rho^\alpha (\partial_x^\beta \rho)^\gamma \quad (\text{S34})$$

where the coupling constants $\lambda_{\alpha\beta\gamma}$ scale as $\mu^{y_{\alpha\beta\gamma}}$ with

$$y_{\alpha\beta\gamma} = 2(2 - \alpha - \gamma) - \beta\gamma. \quad (\text{S35})$$

For $\alpha, \beta, \gamma \geq 1$, $y_{\alpha\beta\gamma} < 0$, so the effect of puff suppression and pushing, at least at large scales is irrelevant and should not change the universality class of the transition from DP.

V. NUMERICAL SIMULATIONS OF THE PUFF-SPLITTING MODEL

To verify these predictions, we have performed numerical simulations. The RG calculation reveals the asymptotic critical scaling, but in practice there might be slow crossovers to the true critical behavior, due to the finite length of a pipe and the finite time for sampling puff dynamics. These effects will be acute near any putative critical point, and so it is important to be able to predict how these effects will be manifested in experiments and simulations. In addition, the divergence of the relaxation time near the critical point means that simulations may be biased by long-lived transients, and these need to be taken into account also.

To rule out sensitive dependence on the numerical implementation, two different computer codes with different update rules and parameter sets were used to check the results. In the first, a minimal discrete model was used to check numerically the conclusions based on perturbative RG arguments given above. In the second, a continuum stochastic dynamics simulation was performed, with a greater level of realism regarding the interactions between the puffs, as determined experimentally. In both simulations, we observe the emergence of a jammed or crystalline phase above the turbulence transition due to the ‘‘traffic jams’’ experienced by puffs. As the transition is approached from higher Reynolds numbers, the crystalline phase effectively melts due to strong fluctuations through the appearance of interspersed disordered regions. Both simulations, when analysed properly, show that the asymptotic universality class is directed percolation, but we identify strong artifacts that complicate the direct observation in experiments of the asymptotic critical scaling.

A. Lattice model of puff dynamics

In order to understand in detail how the phase diagram of interacting puffs depends on individual puff splitting and decay rates, we constructed an additional minimal model that we call the lattice model to differentiate it from the continuum minimal described in the main text.

This minimal model is a computationally-efficient lattice model of the puff interaction dynamics uncovered in our experiments, closely related to the statistical hydrodynamics model. This model permits even greater scale-up than the continuous puff model, and allows us to readily scan through the respective strengths of each interaction and quantify its effects on the DP scaling. In the coarse grained model, we simulate the puff motion by right hopping particles, which push and suppress neighbors and split and decay similarly to the rules described above and explained in the SI. Near the critical point, the puff density is low and τ_d and τ_s are both much larger than the time it takes for a puff to diffuse a distance similar its spatial extent. Thus we can ignore the puff motion below 12D and use this scale as our fundamental lattice unit and the step size for the puff hopping.

1. Detailed description of lattice model

The discrete model consists of a lattice of length L . The dynamics is controlled by a set of parameters

ω_s	the puff splitting rate
ω_d	the puff decay rate
p	the puff hopping rate
λ_{push}	pushing length-scale
q_{sup}	suppression parameter for puffs within a distance λ_{push}
q_{push}	pushing parameter for puffs within a distance λ_{push}

In the basic version of the model, particles hop to the right with a probability p in each time step. We permit puff suppression by allowing a right hopping particle to invade an occupied neighboring site and thereby eliminate a downstream puff/particle. Note that we have also considered a variant of the model where we do not permit puff suppression, meaning that particles do not hop if there would be a collision with an already occupied site. The lifetime $\tau_{d,\infty}$ and time between splitting events, $\tau_{s,\infty}$, are given by a phenomenological fit to experimental data

$$\tau_d(\text{Re}) = \exp[\exp(0.005898 \text{ Re} - 9.1871)],$$

The corresponding expression for the splitting rate is given by

$$\tau_s(\text{Re}) = \exp[\exp(-0.003165 \text{ Re} + 9.2871)].$$

The simulation of the model is performed using one of two update rules, an upstream update rule, where the puffs

in each time step are updated sequentially from the left to the right and a stochastic update rule (producing similar results (in almost all circumstances)) where puffs are picked randomly one-by-one and updated accordingly.

The dimensionless diffusion constant D of the right hopping process is

$$\tilde{D} = \frac{p(1-p)}{2}$$

2. Puff-pushing and suppression

The puff-pushing alters the hopping probability p of a puff x_i depending on the distance $|x_i - x_{i-1}|$ to an upstream puff x_{i-1} . If that distance is smaller than some pushing length λ_{push} , the hopping probability is set to one. Thus, the hopping probability of a puff at x_i is p if $|x_i - x_{i-1}| > \lambda_{push}$ and $q_{push} = 1$ otherwise. Similarly, we use the following expression for the probability of puff-suppression: when a puff is within a distance $d < d_{sup}$ from an upstream puff, the suppression probability at x_i is zero if $|x_i - x_{i-1}| > \lambda_{push}$ and q_{sup} otherwise. For the phase diagram of the puff density in the main paper, $q_{sup}=2e-5$.

3. Comparison to experimental values

In this section, we show how to relate the parameters in the discrete model to those in the experiments and continuous model. The experiments have the following characteristic parameters

D^*	4e-3 m
U^*	0.4995 ms ⁻¹
L^*	6.3e-5 m ² s ⁻¹
T^*	8e-3s = $(D^*)/(U^*)$

In the experiments, a puff has a spatial extent of $\lambda = 12D^*$. For a pipe of length $7800D$ and with a pushing zone reaching out to $\lambda_{push} = 4\lambda$, a system being in the perfect puff-crystal state would contain around $7800/48 = 162$ puffs. If we convert these numbers to units of the discrete model, the corresponding system size would be $162\lambda_{push}/\lambda$ lattice units. We can perform meaningful simulations down to values of $\lambda_{push} = 2\lambda$ i.e. a discrete system representing the experimental system would consist of around 350 lattice units.

Regardless of the model, the scaling of the dimensionless variables should result in the same variables with dimensions, e.g.

$$L^* = \frac{p(1-p)}{2} \frac{\lambda^2}{\tau} \quad (\text{S36})$$

Here λ is a characteristic length scale and τ a characteristic time scale for the model.

All the relevant timescales in the model are scaled with this length and time, where e.g. dimensionless reaction rates become

$$\omega_{\text{decay}}(\text{Re}) = \frac{\tau}{\tau_{\text{decay}}(\text{Re})}$$

$$\omega_{\text{split}}(\text{Re}) = \frac{\tau}{\tau_{\text{split}}(\text{Re})}$$

The scale parameters are determined by matching the model to the characteristics of the experiment. First we choose our length scale to be as large as possible without losing the microscopic details, e.g. the length scale should be smaller than the pushing distance such that puff-pushing is resolved. Here we choose

$$\lambda = 12 D^*,$$

i.e. the spatial extent of a puff. We choose $p = 0.5$ and therefore our timescale follows from equation (S36),

$$\tau = \frac{p(1-p)\lambda^2}{2L^*}. \quad (\text{S37})$$

Note that it is computationally advantageous to use as large as possible a diffusion constant, which would mean $p = 0.5$.

With this choice of parameters, a puff would at $\text{Re} = 2039$ diffuse a length ℓ_d between splitting or decaying events,

$$\ell_d = \lambda \sqrt{p \frac{\tau_d(\text{Re}_c)}{\tau}} = 4900\lambda = 19m \quad (\text{S38})$$

or $\Delta t = 5 \cdot 10^7 \tau = 1.2 \cdot 10^8 s$. At $\text{Re} = 2050$, the scales separating the splitting events are $\Delta t = 2.4 \cdot 10^7 \tau$ and $\ell_d = 1744\lambda$.

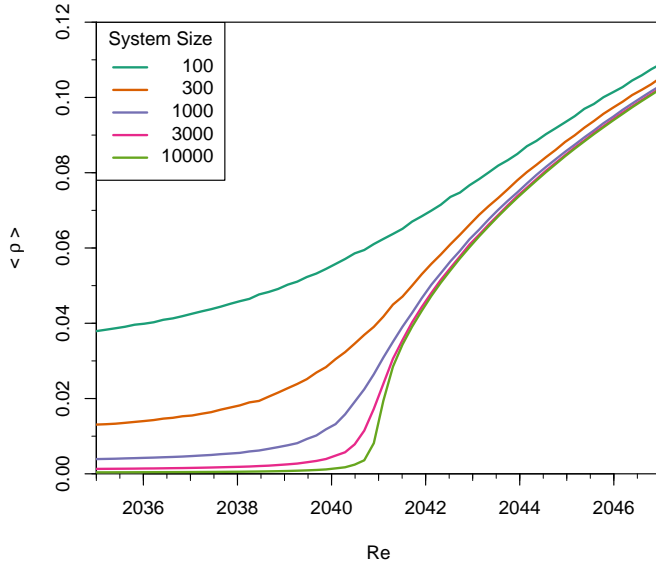


FIG. S6 Numerical simulations of the average density in the lattice model for different values of the system size L .

4. Finite-size analysis in the lattice model

It is well established that to overcome the difficulty of identifying the critical point and measuring critical exponents in simulations one should use finite-size scaling [18, 20]. In this section, we perform finite-size scaling analysis on the lattice model by adopting the procedure in the contact process model by Tomé and de Oliveira [21]. The idea is to remove the absorbing state by forbidding the last particle to decay, and therefore the behavior in the subcritical regime becomes continuous and scalable due to the finite-time effect. The density calculated in the numerical simulations as a function of Re is shown in Fig. S6. The scaling relation of the first and the second moment of the density can be written as

$$\langle \rho \rangle = L^{-\beta/\nu_\perp} F(\epsilon L^{1/\nu_\perp}), \quad (\text{S39})$$

$$\langle \rho^2 \rangle = L^{-2\beta/\nu_\perp} \tilde{F}(\epsilon L^{1/\nu_\perp}), \quad (\text{S40})$$

where $\epsilon = \text{Re} - \text{Re}_c$ and F and \tilde{F} are universal functions. Therefore the reduced second-order cumulant

$$U = \frac{\langle \rho^2 \rangle - \langle \rho \rangle^2}{\langle \rho \rangle^2} \quad (\text{S41})$$

is independent of the system size L at the critical point which can be read off in Fig. S7. In the figure, we see that the reduced second-order cumulant starts to intersect at a unique Re for large enough values of Re , as expected by theory.

The stationary probability in the scaling form becomes

$$P(\rho, \epsilon, L) d\rho = F_P(\rho L^{\beta/\nu_\perp}, \epsilon L^{1/\nu_\perp}) L^{\beta/\nu_\perp} d\rho, \quad (\text{S42})$$

where the universal function F_P shows data collapse in the numerical simulations (Fig. S8). Therefore from the identified critical point, the critical exponent for the density in the lattice model is confirmed to be same as the $1 + 1$ DP as shown in Fig. S9.

We performed the numerical simulations on a periodic lattice of length L (see Fig. S10). In addition to the nearest-neighbor rules *propagation*, *decay* and *splitting* described above, additional rules are implemented modeling *suppression* and *pushing*. Specifically, in each time step all puffs on the lattice are submitted randomly to one of three actions, move, split and decay. After we have picked a given action, we execute it with a probability computed from predefined rates. The move shifts a puff on site i one lattice unit ahead at a rate p provided that the site $i + 1$ is vacant. A splitting event of a puff on site i introduces a new puff either at site $i + 1$ or site $i + 2$ with pre-defined rates ω_s and ω_{push} , respectively. The push is only possible if the sites $i + 1$ and $i + 2$ are vacant. Please note that we could instead have introduced the new puff on either of the sites $i - 1$ or $i - 2$ without changing quantitatively the dynamics. A puff on a site i decays with a rate ω_d if the site $i + 1$ is vacant. Otherwise it decays at a higher rate $\tilde{\omega}$. We then performed

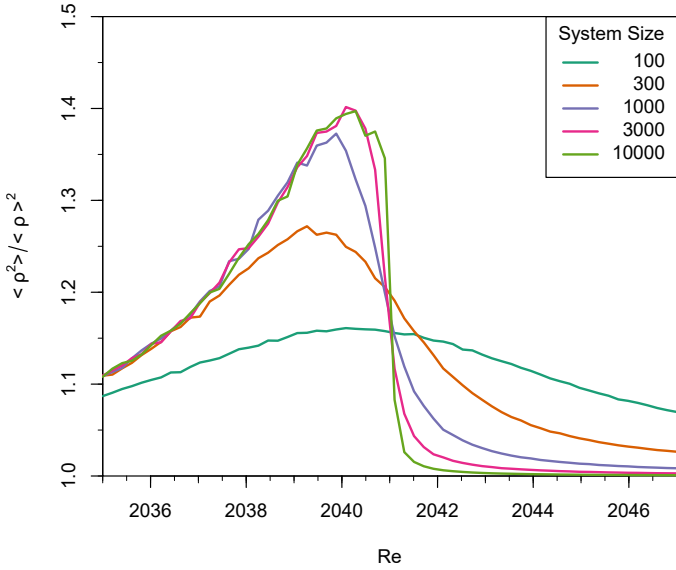


FIG. S7 The reduced second-order cumulant calculated in the numerical simulations of the lattice model as a function of Re and system size L . For sufficiently large L , the curves all intersect at a unique value of Re , thus identifying the actual critical Re that would occur in an infinite system. which is independent of the system size at the critical point. The first and second order moments were computed by averaging over 10^7 time steps after an initial transient of $5 \cdot 10^6$ time steps.

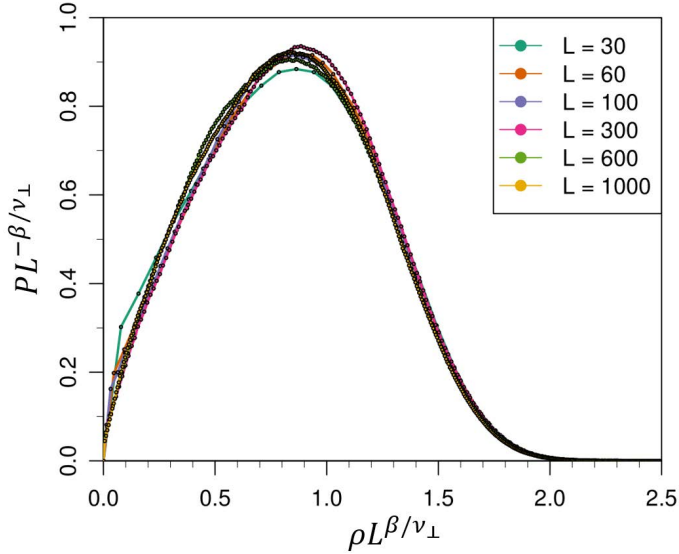


FIG. S8 Data collapse of rescaled probability density in the numerical simulations of the lattice model. The probability was estimated by sampling over 10^7 time steps and after an initial transient of $5 \cdot 10^6$ time steps

the simulations for different systems sizes and for a given number of time steps. We output the density of puffs on the lattice at regular time steps and check whether the system has collapsed into the absorbing state. We also take care to remove long-lived transients, and only take data once the transients have decayed. This required us

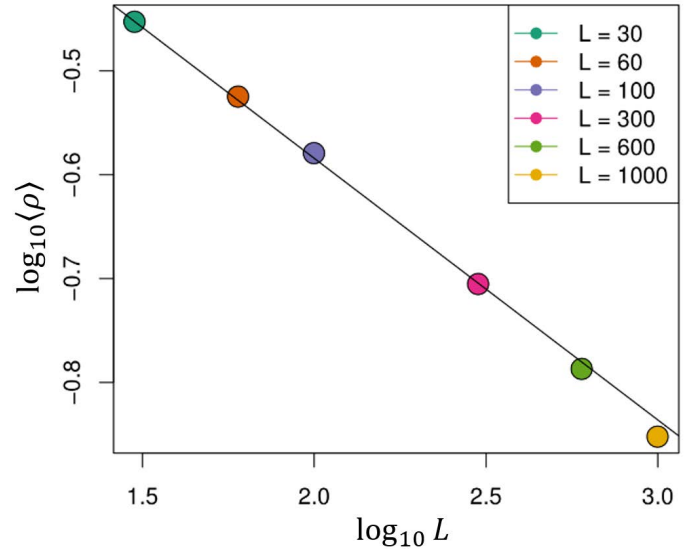


FIG. S9 The average density at the critical point in the numerical simulations of the lattice model. The fitted solid line has a slope of $-\beta/\nu_{\perp}$ with $\nu_{\perp} \sim 0.109$ which is consistent with the known critical exponents of $1+1$ DP. The average density was computed from the simulations presented in Fig. S8.

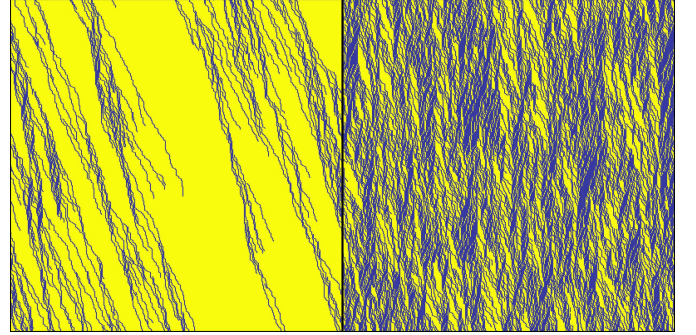


FIG. S10 Numerical simulations of the lattice model for systems respectively below (left panel) and above (right panel) the critical point. Clearly visible above the critical point are traffic jams of puffs, forming a crystalline phase, interspersed with regions of disordered puffs. As the transition is approached from above, the disordered eventually dominate, leading to the pure DP behavior at the critical point. In these simulations, $\omega_d = \tilde{\omega} = 0.01$, $p = \tilde{p} = 0.5$, and $\omega_{push} = \omega_s$ with $\omega_s = 0.0175$ in the left panel and $\omega_s = 0.0375$ in the right panel.

to run as much as 10^7 time steps before equilibration, when close to the transition.

The results of our simulations are summarized in Fig. S11. The turbulent fraction ρ varies with the splitting rate $(\omega_s - \omega_c)^\beta$ with $0.27 < \beta < 0.285$, consistent with the expectation from DP. We have verified that the puff dynamics is in a range where there are strong pushing and “traffic jam” effects.

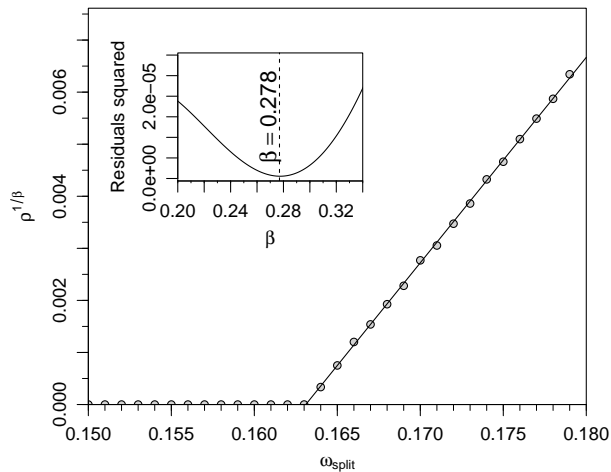


FIG. S11 Turbulent fraction ρ as a function of splitting rate, for a system size $L = 3200$ and averaged over 400 simulations and after a transient of $T = 10^7$ time steps. The vertical axis is the turbulent fraction $\rho^{1/\beta}$ where β has been estimated by a linear model whose residual is shown as function of β in the inset. The value of $\beta = 0.278$ used in the vertical axis varies slightly but has a sample variation in the range 0.270 to 0.285, which is consistent with the known value $\beta \approx 0.276$ for DP. In these simulations, $\omega_d = 0.04$, $\tilde{\omega} = 0.2$, $p = r = 0.5$, and $\omega_{push} = \omega_s$ as on the abscissa.

B. Continuum model of puff dynamics

In our *continuum model*, each puff is considered a point particle interacting with its closest neighbors, using the measured effective potential between puffs. We solve the equation of motion for each puff in the frame co-moving at v_∞

$$\frac{dx_i}{dt} = v_{\text{puff}}(x_i - x_{i-1}) + \sqrt{2D_{\text{puff}}}\xi_i(t) \quad (\text{S43})$$

where x_i is the streamwise coordinate of the i^{th} puff, $v_{\text{puff}}(x_i - x_{i-1})$ is the pushing speed of puff i as a result of puff $i - 1$ as measured in (S44), and $\xi_i(t)$ is a Gaussian white noise with mean zero and standard deviation 1, thus modeling the random walk of an isolated puff with an effective diffusion coefficient D_{puff} . In addition to equation (S43), each puff experiences decay and splitting with rates $\tau_{d,i} = \tau_d(\text{Re}, x_i - x_{i-1})$ and $\tau_{s,i} = \tau_s(\text{Re}, x_{i+1} - x_i)$ respectively, accounting for the presence of an upstream/downstream puff as measured in the experiment.

The pushing speed, v_{puff} , is well-described by an exponential decay:

$$v_{\text{puff}}(l) - v_\infty = A \exp(-l/l_c), \quad (\text{S44})$$

with $A = 0.22$, $l_c = 12$ and v_∞ is the travelling speed of an isolated puff.

1. Puff diffusion coefficient

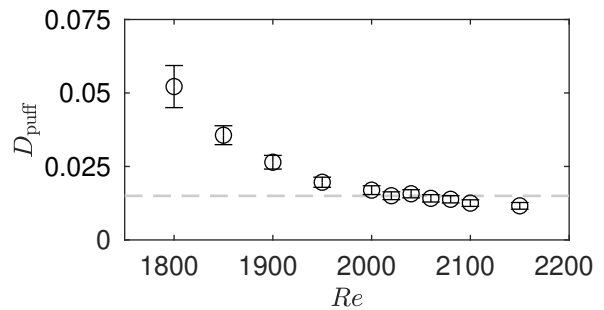


FIG. S12 Evolution of the effective diffusion coefficient versus Re . The dashed line indicates the choice made for the simulation of the continuous model. The diffusion coefficient is estimated from the evolution of the variance of the time of arrival distribution of 1000 puffs. Data are represented by their best fit \pm their 95% confidence interval.

Measuring the evolution of the arrival time distribution at various location, we have been able to confirm that the puff propagation is purely diffusive. We could therefore measure an effective diffusion coefficient D_{puff} for various Re (Fig. S12). This diffusive coefficient is decreasing with Re before reaching a plateau for $\text{Re} \gtrsim 2000$. The higher value for low Re is understood in terms of puff stability. For $\text{Re} = 1800$, a puff will experience many near-relaminarization events before eventually relaminarizing. During such events, the puff energy will decrease substantially and its speed will increase accordingly. This translates into an increased diffusion coefficient. In the transitional range ($2000 < \text{Re} < 2100$), the puff diffusion coefficient is nearly constant around $D_{\text{puff}} = 0.015$ (dashed line in Fig. S12) and therefore, for simplicity, we have chosen not to use a Re -dependent diffusion coefficient in the model and used the value which is approximately constant for the range of Re of interest here.

2. Life and splitting times

A key feature of turbulent puff in pipe flow is their memoryless nature, ie. their life and splitting time statistics follow an exponential distribution. It is therefore possible for each Re to define a characteristic life and splitting time. Experiment [22] indicates that these times for the decay and splitting of an isolated puff depend on Re super exponentially, a result in agreement with theoretical expectations [23] (for a summary of recent work, see [24]). Here, we determine how the presence of a neighboring puff changes these statistics.

We measured puff lifetime and splitting time distributions for puff trains with different spacing and checked that each distribution remains exponential. Fig. S14.a shows the evolution of the life time (circle) and splitting time (square) with Re for different puff to puff dis-

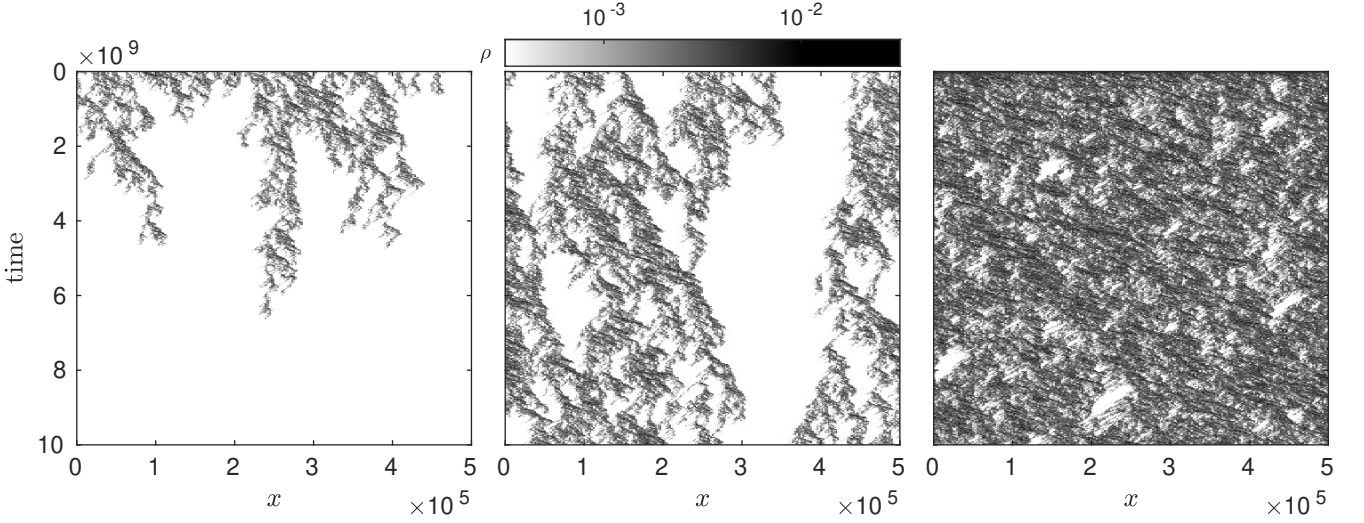


FIG. S13 Spacetime plots of the local puff density ρ at (from left to right) increasing Reynolds numbers for the continuous numerical model. Left panel shows subcritical behaviour ($Re = 2040.0$), while central panel is at $Re = 2040.22 \sim Re_c$ and right panel is above the critical point ($Re = 2040.6$).

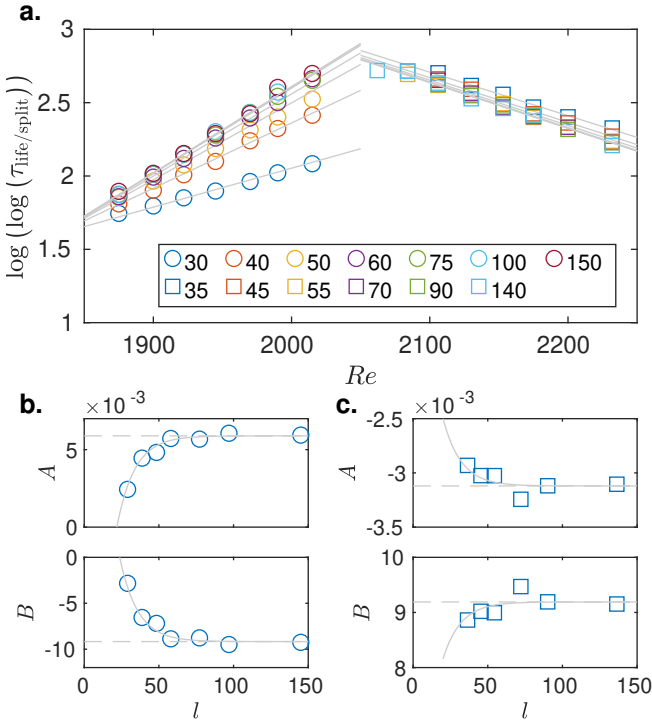


FIG. S14 a. Lifetime (circles) and splitting time (square) for various puff-to-puff distances l . Solid lines indicates a super-exponential fit to the data. **b.** Coefficient A and B of the super exponential fit $\log(\log(\tau)) = A Re + B$ for life times. **c.** Coefficient A and B of the same super exponential fit for splitting times.

tances, l . We note that for each l the Re dependence remains super exponential. For each spacing we fit the Re dependence as $\log(\log(\tau)) = A Re + B$. Fig. S14.b

and S14.c show the dependence of A and B with l for decay and splitting respectively. In both cases we decided to fit it with an exponentially decaying function $A - A_\infty \propto \exp(-l/l_c)$ where $l_c = 12$ was chosen to correspond to the characteristic distance identified in the pushing interaction, in order to limit the number of free parameters.

Eventually, the fit was done using a global non-linear fit on all data using the fitting function

$$\log(\log(\tau)) = (A_\infty + A \exp(-l/l_c)) Re + (B_\infty + B \exp(-l/l_c))$$

where $l_c = 12$ was imposed. The best fit gave the following values where superscript l , and s respectively stand for lifetime and splitting time.

$$\begin{aligned} A_{\infty,l} &= 5.898 \cdot 10^{-3} & A_{\infty,s} &= -3.165 \cdot 10^{-3} \\ B_{\infty,l} &= -9.187 & B_{\infty,s} &= 9.287 \\ A_l &= -3.687 \cdot 10^{-2} & A_s &= 4.714 \cdot 10^{-3} \\ B_l &= 67.45 & B_s &= -8.583 \end{aligned}$$

Representative spacetime plots of the puff configurations for increasing Re are shown in Fig. S13. The extreme sensitivity of the puff density to Re is evident, reflecting the fact that the critical region for the laminar-turbulent transition is very small.

The A_∞ and B_∞ coefficients are to be compared with those found in Avila *et al.* [22]. Although slightly different, they remain within the error bars and were the ones we used for building the model. This anecdotal and seemingly minor difference has actually far reaching consequences as it changes the Reynolds number Re_x where life and splitting times are equal. As a consequence, it dictates the value of the DP critical Reynolds number Re_c . This makes a direct comparison with experimental data extremely sensitive to the values of Re_x and explains the shift we had to impose in Fig. 3.a of

the main paper. Here, we should emphasize the difference between *accuracy* and *precision*. While it is easy to get reproducible experimental conditions when controlling temperature within a fraction of a degree and using the same experimental set-up, it is difficult to ensure absolute accuracy across different experiments. This has various causes such as absolute calibration of temperature sensors and accuracy of glass tubing. Once acknowledged, the agreement between the continuous model and the experimental turbulent fractions (measured in a different set-up) is excellent.

Finally, the choice of the fitting function is not unique and has no physical support other than being short range and therefore decaying exponentially. We have tested other fitting functions such as error functions but did not find any qualitative differences. Therefore the main outcome from the continuous model, the DP phase transition, is robust with respect to the functional form we choose to fit our experimental data.

3. Significance and details on errors estimation

Life time and splitting time for a given (Re, l) pair is estimated by fitting a Poisson distribution to the survivability/splitting distribution. The number of puffs used to build the distribution is given in tables I and II. The error is estimated by calculating the 95% confidence interval of the fit.

Re	l	τ_{life}	$\Delta\tau_{\text{life}}$	N_{puff}
1875	30	3.06e+02	1.91e+02	3900
1875	39	4.50e+02	9.12e+01	4800
1875	50	5.93e+02	5.40e+01	4500
1875	59	6.12e+02	4.87e+01	4500
1875	79	6.80e+02	5.00e+01	4600
1875	99	6.71e+02	1.44e+01	4600
1875	149	7.77e+02	2.68e+01	4600
1900	29	4.13e+02	4.65e+02	3300
1900	39	8.17e+02	2.19e+02	3600
1900	49	1.26e+03	8.91e+01	3500
1900	59	1.53e+03	1.24e+02	3400
1900	79	1.76e+03	1.22e+02	3200
1900	98	1.79e+03	1.72e+02	3000
1900	148	1.85e+03	9.98e+01	4400
1922	29	5.83e+02	7.70e+02	4400
1922	39	1.72e+03	2.23e+02	5100
1922	49	2.90e+03	5.45e+02	5100
1922	59	4.14e+03	4.15e+02	4800
1922	78	5.30e+03	4.03e+02	4600
1922	97	5.30e+03	4.48e+02	4900
1922	147	5.51e+03	3.19e+02	3900
1945	29	7.88e+02	8.83e+02	5000
1945	39	3.50e+03	4.55e+02	4200
1945	48	7.43e+03	2.09e+03	5100
1945	58	1.43e+04	3.55e+03	6000
1945	77	1.75e+04	2.18e+03	5000
1945	97	2.19e+04	2.97e+03	5000
1945	145	1.93e+04	9.59e+03	5600
1970	29	1.23e+03	8.95e+02	8300
1970	39	1.20e+04	3.66e+03	7200
1970	48	2.48e+04	7.09e+03	7000
1970	57	5.83e+04	1.27e+03	7000
1970	76	8.90e+04	6.55e+03	7000
1970	95	8.58e+04	9.98e+03	5000
1970	144	8.08e+04	7.94e+04	4900
1990	29	1.90e+03	8.38e+02	14600
1990	38	2.73e+04	8.20e+03	14300
1990	48	6.30e+04	3.33e+04	11000
1990	57	1.98e+05	5.81e+04	17000
1990	76	3.35e+05	1.52e+05	17000
1990	95	4.89e+05	1.64e+05	18000
1990	142	7.40e+05	6.20e+05	12200
2015	29	3.09e+03	7.87e+02	12600
2015	38	7.17e+04	2.18e+04	12100
2015	47	2.64e+05	2.11e+05	12000
2015	57	1.70e+06	5.36e+05	12000
2015	75	1.45e+06	1.20e+06	12000
2015	141	2.85e+06	2.39e+06	13000

TABLE I Details of the statistical analysis for measuring the life time of a puff. N_{puff} corresponds to the number of puffs generated to build the survivability distribution.

Re	l	τ_{split}	$\Delta\tau_{\text{split}}$	N_{puff}
2084	46	3.63e+06	1.33e+06	47000
2084	56	2.61e+06	1.10e+06	44000
2084	139	3.58e+06	3.01e+06	32000
2106	37	3.05e+06	1.49e+06	41000
2106	46	1.65e+06	1.11e+06	41000
2106	55	9.00e+05	1.73e+05	38000
2106	73	1.45e+06	9.93e+05	21000
2106	92	9.76e+05	3.41e+05	20000
2106	138	1.11e+06	2.33e+05	28000
2130	37	8.84e+05	2.66e+05	31000
2130	46	6.26e+05	2.94e+05	30000
2130	55	3.99e+05	2.90e+05	26000
2130	73	4.41e+05	1.68e+05	11000
2130	91	3.56e+05	1.57e+05	11000
2130	137	2.72e+05	1.31e+05	8000
2153	37	3.97e+05	1.62e+05	15000
2153	45	1.75e+05	6.11e+04	15000
2153	54	1.80e+05	5.82e+04	15000
2153	72	1.36e+05	2.36e+04	5000
2153	90	1.63e+05	1.56e+04	5000
2153	136	1.22e+05	6.73e+03	5000
2175	36	1.36e+05	5.56e+04	5000
2175	45	8.01e+04	3.52e+04	5000
2175	54	6.12e+04	6.58e+03	5000
2175	72	6.49e+04	2.03e+04	5000
2175	90	6.93e+04	1.16e+04	5000
2175	135	7.34e+04	2.50e+04	5000
2200	36	6.34e+04	9.86e+03	5000
2200	45	4.06e+04	6.26e+03	5000
2200	54	2.94e+04	5.03e+03	5000
2200	72	2.99e+04	9.44e+02	5000
2200	89	2.57e+04	4.12e+03	5000
2232	36	2.82e+04	1.33e+04	3000
2232	45	1.62e+04	4.34e+03	3000
2232	54	1.18e+04	1.57e+03	4900
2232	71	1.09e+04	1.12e+03	4900
2232	89	1.06e+04	1.02e+03	4900
2232	134	8.93e+03	3.68e+03	4900
2261	36	1.26e+04	4.08e+03	1000
2261	45	7.68e+03	4.16e+02	1000
2261	54	6.09e+03	1.59e+03	4900
2261	71	5.14e+03	5.12e+02	4800
2261	89	5.28e+03	9.39e+02	4900
2261	133	4.90e+03	8.57e+02	4900

TABLE II Details of the statistical analysis for measuring the splitting time of a puff. N_{puff} corresponds to the number of puffs generated to build the splitting distribution.

Re	ρ	ρ_{min}	ρ_{max}	Δ_t	N
2040.21	1.51e-04	9.72e-05	2.41e-04	5.0e+11	499998
2040.22	5.61e-04	4.94e-04	6.34e-04	5.0e+11	499998
2040.23	7.10e-04	6.32e-04	7.94e-04	3.9e+11	386701
2040.24	8.54e-04	6.39e-04	1.11e-03	2.5e+11	249999
2040.26	9.93e-04	8.21e-04	1.19e-03	2.0e+11	199998
2040.28	1.16e-03	9.70e-04	1.34e-03	2.0e+11	199998
2040.30	1.25e-03	1.09e-03	1.41e-03	5.0e+10	49999
2040.40	1.64e-03	1.52e-03	1.79e-03	3.5e+10	34877
2040.50	1.92e-03	1.81e-03	2.05e-03	1.5e+10	15316
2040.60	2.15e-03	2.05e-03	2.28e-03	9.3e+09	9324
2040.70	2.39e-03	2.29e-03	2.50e-03	7.4e+09	7422
2040.80	2.61e-03	2.51e-03	2.71e-03	5.0e+09	5018
2040.90	2.79e-03	2.68e-03	2.88e-03	3.4e+09	3414
2041.00	3.00e-03	2.94e-03	3.07e-03	1.7e+09	1692
2042.00	4.49e-03	4.41e-03	4.58e-03	1.3e+09	1279
2043.00	5.67e-03	5.60e-03	5.73e-03	1.2e+09	1165
2044.00	6.61e-03	6.53e-03	6.67e-03	1.0e+09	1031
2045.00	7.43e-03	7.36e-03	7.50e-03	9.3e+08	931
2046.00	8.12e-03	8.05e-03	8.17e-03	7.5e+08	752
2047.00	8.73e-03	8.68e-03	8.79e-03	6.7e+08	669
2048.00	9.26e-03	9.21e-03	9.33e-03	6.4e+08	644
2049.00	9.76e-03	9.72e-03	9.82e-03	6.1e+08	606
2050.00	1.02e-02	1.01e-02	1.03e-02	5.1e+08	514
2052.00	1.10e-02	1.09e-02	1.10e-02	4.6e+08	464
2055.00	1.20e-02	1.19e-02	1.20e-02	4.2e+08	420
2060.00	1.32e-02	1.32e-02	1.33e-02	3.7e+08	371
2065.00	1.42e-02	1.42e-02	1.42e-02	3.4e+08	340
2070.00	1.50e-02	1.50e-02	1.51e-02	3.5e+08	349
2080.00	1.63e-02	1.63e-02	1.64e-02	3.3e+08	328
2090.00	1.74e-02	1.74e-02	1.74e-02	2.8e+08	282
2100.00	1.82e-02	1.82e-02	1.83e-02	3.4e+08	342

TABLE III Details of the statistical analysis for measuring the equilibrium puff density ρ . The puff density is time averaged with Δ_t the duration of the interval and N the number of samples.

VI. DATA AND CODE AVAILABILITY STATEMENT

All experimental and computational data presented in this paper, the codes used to generate those data and the codes and scripts used to generate the figures are available online in the Zenodo repository [10.5281/zenodo.10308791](https://zenodo.org/doi/10.5281/zenodo.10308791) at <https://zenodo.org/doi/10.5281/zenodo.10308791>

VII. ACKNOWLEDGMENTS

One of us (NG) thanks Uwe Täuber for a useful discussion. GL and JM are thankful to A. Hernandez-Garcia for stimulating discussions.

This work was partially supported by two grants from the Simons Foundation (Grant number 662985, NG) and (Grant number 662960, BH) and by Ministry of Science and Technology, Taiwan (Grant number MOST 109-2112-M-001-017-MY3 and Grant number MOST 111-2112-M-001-027-MY3 (HYS)). Part of this work was performed using computing resources of CRIANN (Normandy, France).

Correspondence to Björn Hof (bhof@ist.ac.at) and Nigel Goldenfeld (nigelg@ucsd.edu).

-
- [1] Y. Pomeau, *Physica* **23D**, 3 (1986).
 - [2] H.-Y. Shih, T.-L. Hsieh, and N. Goldenfeld, *Nature Physics* **12**, 245 (2016).
 - [3] N. Goldenfeld and H.-Y. Shih, *Journal of Statistical Physics* **167**, 575 (2017).
 - [4] X. Wang, H.-Y. Shih, and N. Goldenfeld, *Phys. Rev. Lett.* **129**, 034501 (2022).
 - [5] D. Barkley, B. Song, V. Mukund, G. Lemoult, M. Avila, and B. Hof, *Nature* **526**, 550 (2015).
 - [6] D. Barkley, *Journal of Fluid Mechanics* **803** (2016).
 - [7] V. Mukund and B. Hof, *Journal of Fluid Mechanics* **839**, 76 (2018).
 - [8] B. Hof, A. de Lozar, D. J. Kuik, and J. Westerweel, *Phys. Rev. Lett.* **101**, 214501 (2008).
 - [9] D. Helbing, *Reviews of Modern Physics* **73**, 1067 (2001).
 - [10] T. Chou, K. Mallick, and R. Zia, *Reports on Progress in Physics* **74**, 116601 (2011).
 - [11] H. Hinrichsen, *Advances in Physics* **49**, 815 (2000).
 - [12] M. Doi, *Journal of Physics A: Mathematical and General* **9**, 1465 (1976).
 - [13] P. Martin, E. Siggia, and H. Rose, *Physical Review A* **8**, 423 (1973).
 - [14] H.-K. Janssen, *Zeitschrift für Physik B Condensed Matter* **23**, 377 (1976).
 - [15] C. d. Dominicis, in *J. Phys.(Paris), Colloq* (1976) pp. C1–247.
 - [16] U. C. Täuber, *Critical dynamics: a field theory approach to equilibrium and non-equilibrium scaling behavior* (Cambridge University Press, 2014).
 - [17] C. Gardiner, *Springer Series in Synergetics*, Berlin: Springer,— c1994, 2nd ed. 1985. Corr. 3rd printing 1994 (1994).
 - [18] N. Goldenfeld, *Lectures On Phase Transitions And The Renormalization Group* (Addison-Wesley Reading, MA, 1992).
 - [19] M. Mobilia, I. T. Georgiev, and U. C. Täuber, *Journal of Statistical Physics* **128**, 447 (2007).
 - [20] J. Cardy, *Finite-size scaling* (Elsevier, 2012).
 - [21] T. Tomé and M. J. de Oliveira, *Physical Review E* **72**, 026130 (2005).
 - [22] K. Avila, D. Moxey, A. de Lozar, M. Avila, D. Barkley, and B. Hof, *Science* **333**, 192 (2011).
 - [23] N. Goldenfeld, N. Guttenberg, and G. Gioia, *Physical Review E* **81**, 035304 (2010).
 - [24] S. Gomé, L. S. Tuckerman, and D. Barkley, *Philosophical Transactions of the Royal Society A* **380**, 20210036 (2022).